

DXAI: Explaining Classification by Image Decomposition

Elnatan Kadar

Guy Gilboa

Abstract

We propose a new way to explain and to visualize neural network classification through a decomposition-based explainable AI (DXAI). Instead of providing an explanation heatmap, our method yields a decomposition of the image into class-agnostic and class-distinct parts, with respect to the data and chosen classifier. Following a fundamental signal processing paradigm of analysis and synthesis, the original image is the sum of the decomposed parts. We thus obtain a radically different way of explaining classification. The class-agnostic part ideally is composed of all image features which do not possess class information, where the class-distinct part is its complementary. This new visualization can be more helpful and informative in certain scenarios, especially when the attributes are dense, global and additive in nature, for instance, when colors or textures are essential for class distinction. Code is available at <https://github.com/dxai2024/dxai>.

1. Introduction

Understanding classification reasoning of neural networks is of paramount importance. It can lead to better understanding of the classification process, help in debugging and validation and also serve as an additional informative output for the user at inference. Thus, the research on the topic of explainable artificial intelligence (XAI) is extensive [2, 11, 13, 18].

The most common way to show the explanation of the network in image classification is by producing an *explanation heatmap*. This map is a per-pixel indication of the relevance of that pixel to the final classification decision of the network (see Fig. 2). In this visualization, the larger the value - the more relevant this pixel is to the classification. These maps can be at some lower resolution, where visualization is done by upsampling, or by using superpixels. In addition, some methods give also negative values, indicating pixels which reduce the confidence for the final classification. The heatmaps themselves do not resemble actual images and to understand the role of the pixels in a heatmap common practices are either to show the input image and the heatmap side by side, to overlay the heatmap on the image, or (less commonly) to show an image where the brightness of the

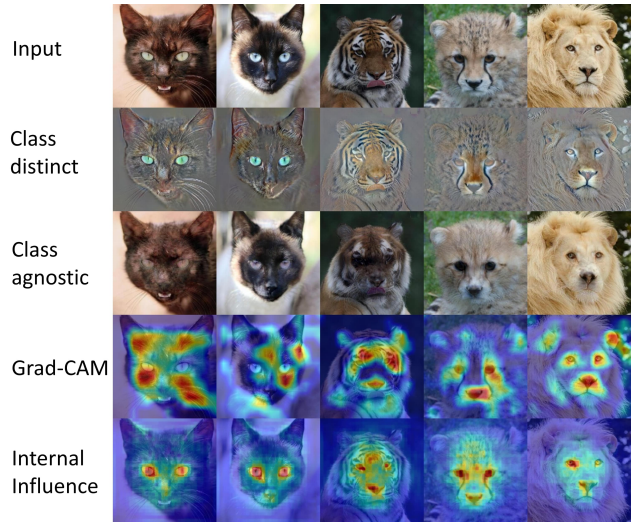


Figure 1. **What makes a cat a Cat? Explained through decomposition.** Examples of class-distinct, $\psi_{Distinct}$, and class-agnostic, $\psi_{Agnostic}$, parts of Animals dataset [8], where the input $x = \psi_{Agnostic} + \psi_{Distinct}$. The distinct part gives high resolution, dense, color and texture information explaining the classification decision. This is in contrast to standard XAI (bottom two rows).

pixels are weighted by the (normalized) heatmap, Fig. 2.

This visual explanation method is mostly adequate when the explanation is spatially *sparse*. That is, there are just a few small regions in the image which contribute mostly to the classification. However, there are many classification problems in which the explanations are *dense* in the image domain. This can happen in several scenarios, for instance:

1. The object to be classified spans a large portion of the image domain and contains many diverse features, all contributing to the final classification.
2. A main feature contributing to the classification is color change, which appears throughout the image.
3. The class distinction is based on some global disturbance or statistical change, which spans the entire image domain.

In such scenarios, a heatmap is much less informative. Depending on the algorithm, it is either too focused on just a small portion of highly dominant features or it shows uniform large areas spanning most of the image. See some ex-

amples in Fig. 3. In both cases, we lack a clear constructive explanation for the network’s decision.

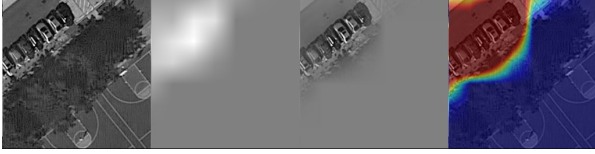


Figure 2. Three visualizations using a heatmap. Generated by Grad-CAM [29], highlighting cars in an aerial image (left).

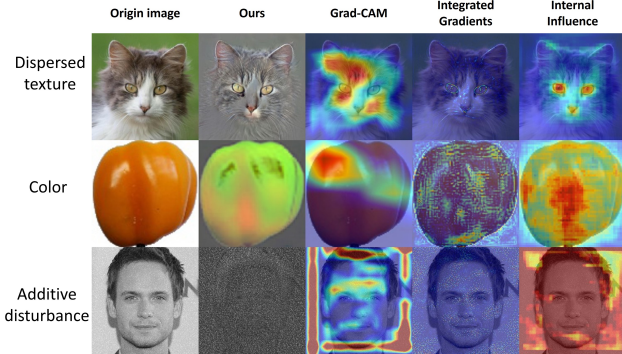


Figure 3. Our method vs. heatmaps, illustrating three scenarios mentioned in Section 1: 1) Many details spread across large portions of the image are helpful for accurate classification (top row), heatmaps show only partial relevant information. 2) Distinguishing between types of peppers that differ mainly by color (2nd row), heatmaps struggle to provide color data. 3) Detecting additive statistical disturbance (a class of clean images and a class of images with noise). Here as well, heatmaps face difficulties explaining the reason for classification.

To alleviate the above problems, we propose a different way of computing and visualizing explanations of the classification. It does not use heatmaps and is based on decomposition. Image decomposition is a long standing paradigm in classical image processing. It is based on the notion that images (and signals in general) can often be well decomposed into meaningful additive parts. Given a 1D signal x of length N and some orthonormal basis of N elements $\{\phi_i\}$, $i = 1, \dots, N$, one can express x as

$$x = \sum_{i=1}^N \alpha_i \phi_i,$$

with $\alpha_i = \langle x, \phi_i \rangle$, where $\langle \cdot, \cdot \rangle$ denotes inner-product. Some well known examples which fall into this category are Fourier and wavelet basis [9, 23]. In overcomplete representations [1, 10] a common practice is to decompose a signal into only a few $K \ll N$ elements (sparse representation) of an overcomplete dictionary $\{\psi_i\}$, $i = 1, \dots, D \gg N$,

allowing some small error e ,

$$x = \sum_{i=1}^K \alpha_i \psi_i + e.$$

There are many other studies attempting to decompose an image into meaningful additive parts. For example, image decomposition into structure and texture $x = \psi_{Structure} + \psi_{Texture} (+e)$ (with possible noise or small error) [3, 4, 12].

In this work we propose to express XAI by the following image decomposition:

$$x = \psi_{Agnostic} + \psi_{Distinct}, \quad (1)$$

where $\psi_{Agnostic}$ is the *class agnostic* part of the image, which ideally does not entail information about the class, and $\psi_{Distinct}$ is the *class distinct* part which holds the discriminative information, allowing the classifier to obtain distinction from other classes. We use style transfer based on generative AI to accomplish this. We show this way of explaining classification brings new computational and visualization tools, which, for some cases, are much more natural and informative. Our main contributions are as follows:

1. We present a detailed computational framework to estimate Eq. (1), for a given classifier, training set and classification task. The decomposition is of high resolution, allowing to portray well fine and delicate details.
2. We show, for the first time, class agnostic images, based on decomposition. This provides new information and insights on the classification problem.
3. The method is fast since results are produced at inference time of generative models (no gradients are computed).
4. We provide extensive examples and experimental data showing the advantages (and limitations) of the method, compared to heatmaps.

2. Related Work

In this work, we focus on visually explaining image classification. Specifically, we concentrate on algorithms that, given an image classification result, highlight the areas contributing to the classification [5, 20–22, 27, 29, 30, 32]. As previously discussed, high values indicate significance, while values near 0 are of negligible contribution. A leading approach is backpropagation-based methods [5, 29, 30]. It involves tracing the classifier’s solution backward through the model’s layers to measure the contribution of each layer to the subsequent one. These methods encompass gradient-based and attribution-based techniques. Perturbation-based methods [22, 27, 32] evaluate the impact on the output of changes in the input. Changes leading to strong output variations are deemed important.

Attention-based methods [14, 20, 35] identify relationships within the input to discern important image characteristics. These methods often require specific classifier architectures. Other methods estimate the uncertainty in the

solution and use this to find explanations with high confidence [24, 37]. Generative models are also used to explain differences between classes. Many of the methods recently try to provide counterfactual explanations [17, 26]. However, it appears to be difficult to use these explanations in order to produce a map of clearly highlighted differences. Current XAI methods typically suffer from at least one of the following drawbacks:

1. **Resolution.** Low resolution that hinders fine detail distinction, usually caused by calculating importance in spatially coarse internal layers.
2. **Compute.** Extended runtime or high memory consumption due to gradient or attribution calculations across multiple layers or using numerous perturbation iterations.
3. **Architecture.** Certain solutions impose architectural constraints, such as specific activation layers or even a dedicated architecture designed solely for XAI.
4. **Single channel.** Typically, these algorithms produce grayscale images representing the importance of each pixel, lacking color distinction (multi-channel data in general). This can lead to inadequate explanations, as seen, for example, in our peppers dataset experiment (Fig. 11).

Our proposed approach comprehensively addresses these challenges, as detailed below.

3. Method

We aim at partitioning the image to a component which is neutral for the classifier (agnostic) and to a component which explains the classification (distinct). We provide some definitions and formulate the DXAI problem. This is a very hard nonconvex minimization problem. In the second part we present an architecture and a training procedure to obtain an approximate solution.

3.1. The DXAI problem

We first introduce the basic setting and notations. We assume a multiclass supervised learning setting. Let X be the space of input images and $x \in X$ be an input image belonging to one of c classes. Let $y \in Y$ be a class label $y \in \{0, c - 1\}$. The training set consists of M pairs $(x_i, y_i) \in X \times Y$, $i = 1, \dots, M$. We denote by x^y an image x belonging to class y . We are given an image classifier C , which provides a class probability vector p . We would like to extract the relevant features, and only them, which contribute to the classification decision by the network. An additive contribution, as in Eq. (1), is assumed. We want to have a reference image, which is neutral in terms of classification (for a given classifier), using the following definition:

Definition 1 (Class Agnostic) For an image $\psi \in X$, given c classes of images and a classifier C providing a vector $p(\psi) \in \mathbb{R}^c$ of class probabilities, ψ is class agnostic if the

probability is uniform, that is $p_i(\psi) = \frac{1}{c}$, $\forall i = 1, \dots, c$, where p_i is the i 's entry of p .

We denote by $X_A \subset X$ the space of all $\psi \in X$ which are class agnostic, as defined above. Given an image $x \in X$ with class probability vector $p(x)$, and a classifier C , we would like to solve the following minimization problem:

$$\min_{\psi \in X_A} d(x, \psi), \quad (2)$$

where $d(\cdot, \cdot)$ is some distance measure. For instance, our implementation uses a combination of L^1 and L^2 norms for this distance. We refer to Eq. (2) as the DXAI (decomposition-based XAI) problem. We can now define the class distinct and class agnostic parts of an image x .

Definition 2 (Class Distinct / Agnostic parts of x) Let $x \in X$ be an image with class probability vector $p(x)$ provided by the classifier C . Let ψ^* be a minimizer of (2). Then $\psi_{Agnostic} = \psi^*$ is a class agnostic part of image x and $\psi_{Distinct} = x - \psi^*$ is a class distinct part.

In words, for a given image x , we find the closest image (with respect to d) which is neutral, in terms of class (agnostic part). The difference between x and this neutral image explains the probability vector $p(x)$ and the reason, according to the classifier, why it deviates from neutrality. We do not assume a unique solution. The pair $\{\psi_{Agnostic}, \psi_{Distinct}\}$ provide detailed and dense class explanation. We note that pure agnostic images are hard to obtain. A more relaxed requirement is to have $|p_i(\psi) - \frac{1}{c}| \leq \varepsilon$, $0 < \varepsilon \ll \frac{1}{c}$ in Def. 1. In any case, problem (2) is very hard to solve. We give below a suggested approximation. Alternative methods may be further investigated.

3.2. Approximate solution for the DXAI problem

Given an image x classified to class y by the classifier C , we want to approximate a pair $\{\psi_{Agnostic}, \psi_{Distinct}\}$. We use generative models for the decomposition. We leverage style transfer as the primary tool for discerning inter-class differences and generating class-explanations. Our implementation uses style-transfer GANs [8]. Following [6], which shows better descriptive capacity of branched GANs, we use several generators for the agnostic part, which usually contains most of the image data. We assume to have n style transfer generators $G_i(x^y, s_y)$, which take as inputs an image x^y and a style vector s_y . The style vector is generated by a dedicated mapping network, as detailed in [8]. This network takes the class as input and produces the corresponding style representation. Given an image x^y of class y we approximate it by the following decomposition into n components (branches):

$$\hat{x}^y = \psi_1^y + \sum_{i=2}^n \psi_i^y, \quad (3)$$

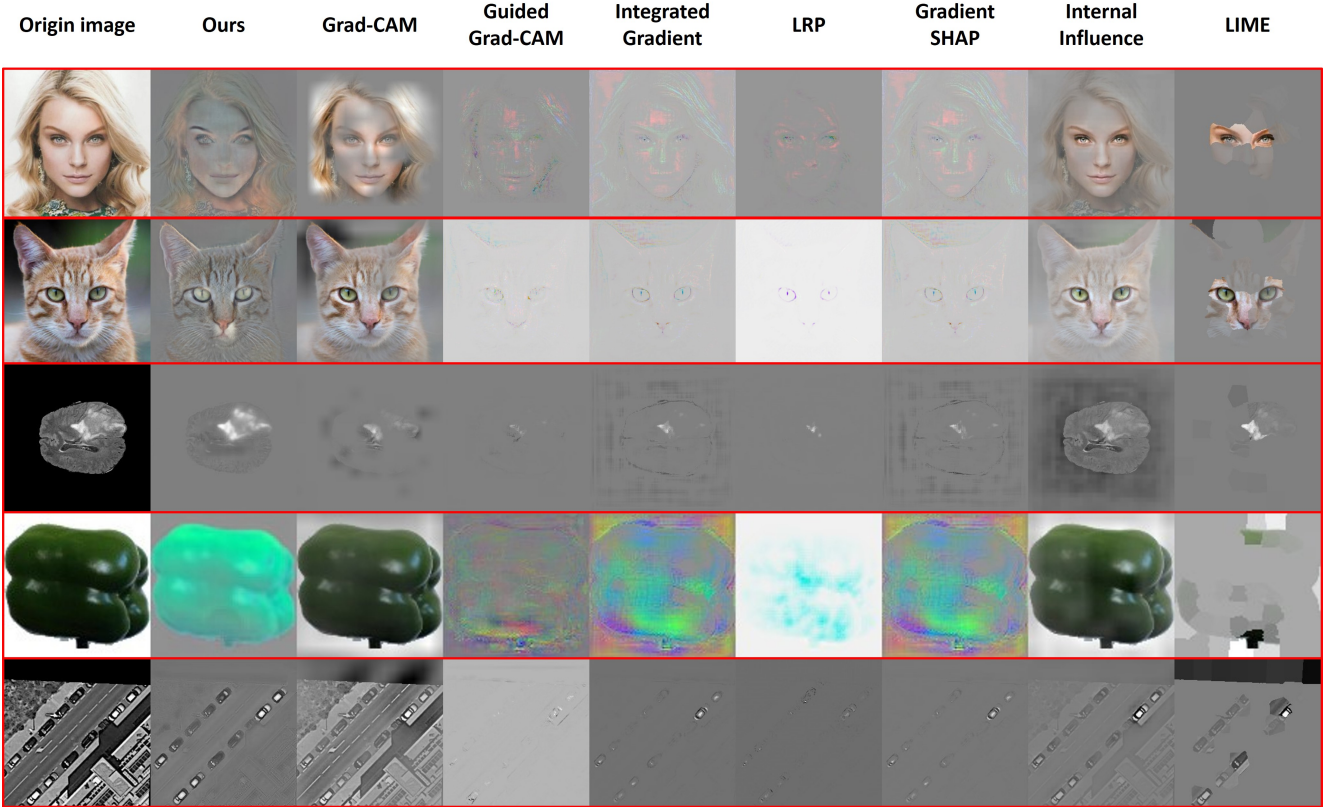


Figure 4. Class-distinct component $\psi_{Distinct}$ by our DXAI algorithm and by heatmap manipulation, in which the input image is weighted by the normalized heatmap (see details in Sec. 4). We obtain high resolution, dense multi-channel explanations.

where $\hat{x}^y \approx x^y$ and $\psi_i^y = G_i(x^y, s_y)$. We assign

$$\psi_{Distinct} = \psi_1^y; \quad \psi_{Agnostic} = \sum_{i=2}^n \psi_i^y. \quad (4)$$

Our aim is to transform an image from class y into an image representative of target class \tilde{y} . Successful style transfer requires the identification and modification of distinct class-specific characteristics. Style transfer is accomplished by using the style vector associated with class \tilde{y} in the generators. That is, $\psi_i^{\tilde{y}} = G_i(x^y, s_{\tilde{y}})$.

In addition, our architecture incorporates a multi-head discriminator (D), a versatile component that serves dual roles within our framework. This discriminator takes an image as input, producing a vector whose length corresponds to the number of classes. Each element in this vector is a “grade”, reflecting the authenticity of the input image concerning the class it represents. Beyond its role as a discriminator, D also serves as a classifier, effectively classifying the input image by selecting the class with the highest “grade” using argmax of its output vector.

Lastly, we have a pre-trained classifier (C), for which DXAI is computed. In this context, the generators aim to de-

ceive the classifier by aligning their outputs with the intended class representation. Here, our multi-head discriminator’s primary function is to evaluate the extent to which the generators successfully mislead the pre-trained classifier while ensuring the overall quality and realism of the generated images.

3.3. Training

We list below the essential training procedure and losses. See Fig. 5 for an overall diagram of the general architecture, consisting of several style-transfer generators, our proposed α -blending procedure, style and quality discriminator and classifier. More details, including ablation studies, appear in the supplementary material.

New α -blended generation. In order for the first channel to contain class distinct information, we propose a novel α -blending mechanism. For each batch, a random vector α of length $n - 1$ is drawn, where each element is uniformly distributed in the range $[0, 1]$. Two images are then generated

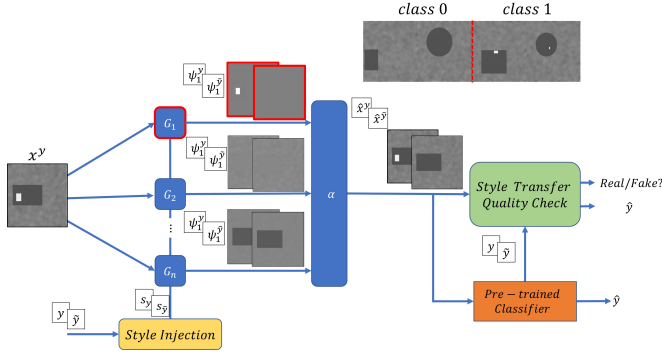


Figure 5. **Training process diagram.** The class distinct part (existence/absence of white rectangle) is in the first branch (top, in red), whereas the class agnostic components, which belong to both classes, are generated by subsequent branches. The α -blended generation is a major mechanism controlling the training.

during training as follows:

$$\begin{aligned}\hat{x}^y &= \psi_1^y + \sum_{i=2}^n \alpha_{i-1} \psi_i^y + \sum_{i=2}^n (1 - \alpha_{i-1}) \psi_i^{\tilde{y}}, \\ \hat{x}^{\tilde{y}} &= \psi_1^{\tilde{y}} + \sum_{i=2}^n \alpha_{i-1} \psi_i^{\tilde{y}} + \sum_{i=2}^n (1 - \alpha_{i-1}) \psi_i^y,\end{aligned}\quad (5)$$

where y is the class of the input image and \tilde{y} represents a random alternative class, $\tilde{y} \neq y$. The proposed method encourages the generators to generate identical images for both components in the sum $\psi_i^y \approx \psi_i^{\tilde{y}}$, $i = 2, \dots, n$, and thus to isolate the distinction between the classes to ψ_1 . In the ideal case, where the components in the sum are identical and the distinction is only in ψ_1 we converge to Eq. (3). The proposed α -blending method allows a stable and effective training. We note that other alternatives, such as attempting to use norm-based losses, e.g. $\|\psi_i^y - \psi_i^{\tilde{y}}\|$, often yield degenerate solutions, with $\psi_i^y \approx 0$.

Classification loss. Since a pre-trained classifier is integrated into our system, there is no need to further train it on authentic images. Instead, we leverage its classification and attempt to explain it. We enable the generators to produce images that correspond to the classifier’s predictions through the following loss function:

$$L_{class-fake} = CrossEntropy\left(C\left(G\left(x^y, s_{y_{trg}}\right)\right), y_{trg}\right). \quad (6)$$

In our GAN-based model, the discriminator is used also as a classifier, in addition to its classical role. This is in order to distinguish between real and fake images in each class. We use a Kullback-Leibler divergence loss between the classification output of the discriminator and that of the pre-trained classifier C . This promotes having a high value in the discriminator output only for images which appear real and fit the correct class.

Reconstruction loss.

Our generated image \hat{x}^y is only an approximation of x , see Eqs. (3), (5). To obtain a good approximation, $\hat{x}^y \approx x$, we use a fidelity measure, based on L^1 and L^2 norms,

$$d(u, v) = \|u - v\|_{L^1} + \|u - v\|_{L^2}, \quad (7)$$

to penalize small and large changes. We would also like the style transferred class to be similar to the input image. Thus, the reconstruction loss is with respect to the generated images of both classes,

$$L_{rec} = d(x, \hat{x}^y) + d(x, \hat{x}^{\tilde{y}}), \quad (8)$$

where $\hat{x}^y, \hat{x}^{\tilde{y}}$ are given in (5).

DXAI and zero distinction. Let us see how the training process and losses above approximate the DXAI problem. The reconstruction loss promotes $x \approx \hat{x}^y \approx \hat{x}^{\tilde{y}}$. The classification loss promotes that $\hat{x}^{\tilde{y}}$ belongs to class $\tilde{y} \neq y$. Thus, the shared components $\psi_i^y \approx \psi_i^{\tilde{y}}$, $i = 2, \dots, n$, should belong to the class-agnostic part. The effects of branch specialization, as shown in [6], encourage each ψ_i to contain different image characteristics. Since class \tilde{y} is random, following (4), we get that $\psi_{Agnostic}$ is not committed to any specific class.

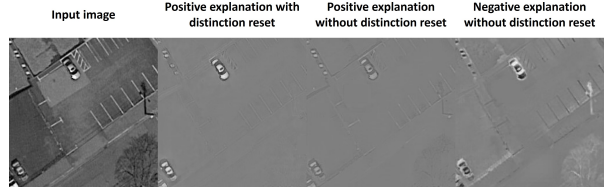


Figure 6. **Effect of resetting the distinction branch.** This reset yields enhanced and cleaner class explanation (cars), in contrast to less prominent and possibly negative explanation otherwise.

In addition, we chose to set $\psi_1^{\tilde{y}} = 0$ in Eq. (5). This is in line with the DXAI formulation, Eq. (2). We would like to choose the agnostic part which is closest to the input image. We explain below additional benefits of this setting. Since our algorithm is of additive nature, it can offer two types of explanations. The more intuitive approach is to highlight unique class features positively, effectively adding distinctiveness to an image with neutral attributes. This ensures the appearance of the differences in the distinction map. Alternatively, it is possible also to *subtract* distinct features. Negative explanations are less preferred, since they are less intuitive for class explanation. For instance, when our classifier predicts an image contains cars, we prefer to receive an image of cars in $\psi_{Distinct}$, rather than a subtraction when it predicts the absence of cars. Setting the distinction of the alternative class to zero diminishes negative explanations. Moreover, this promotes the full network to produce as realistic images as possible by the alternative generators, reducing

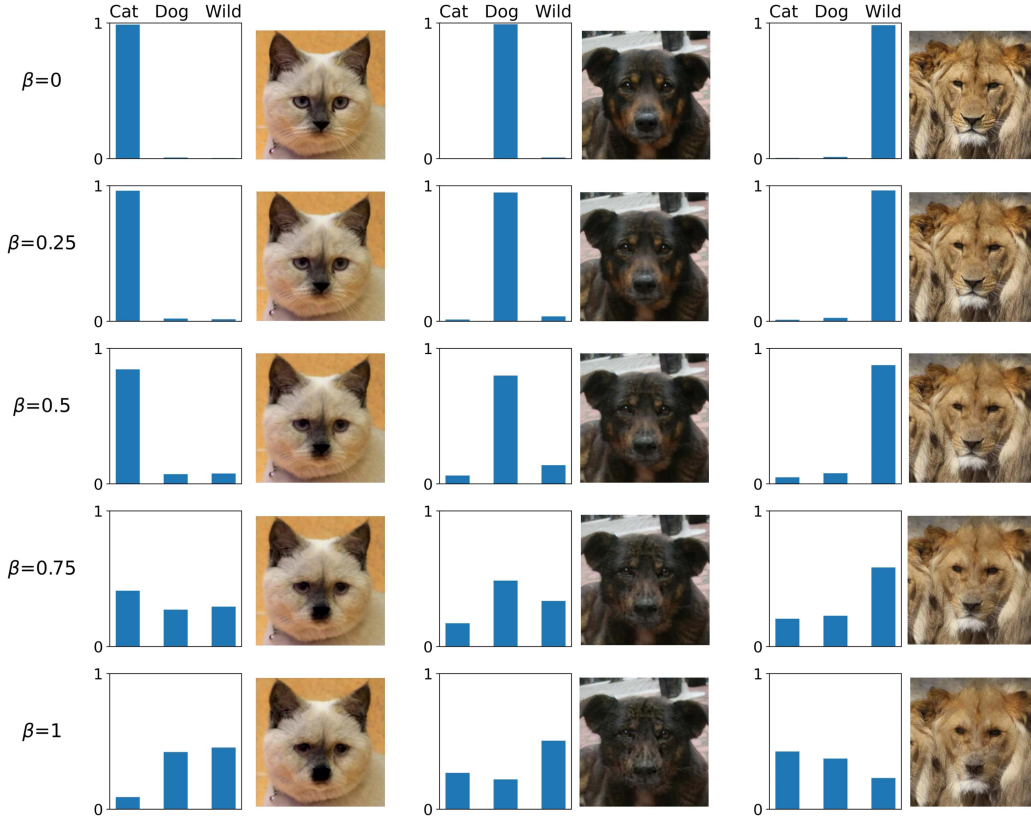


Figure 7. **Linear reduction in class distinction.** We examine the classification results of the following generated images $x_\beta = x - \beta \cdot \psi_{Distinct}$. The bar plots show the average probabilities (softmax output) for each class, from left: Cat, Dog, Wild. An image example of x_β is shown for each class. We observe that as β increases, class distinction decreases, where for $\beta = 1$ we have $x_\beta = \psi_{Agnostic}$. Ideally we should obtain equal probabilities for all classes, we observe our algorithm produces some overshoots toward alternative classes.

spurious features and undesired details in the class-distinct component, see Fig. 6.

Orthogonality loss. We also incorporate a loss function to promote low correlation between branches in the feature space. This loss is defined as:

$$L_{orth} = \sum_{l=1}^L \sum_{i \neq j} (\text{corr}(F_i^l, F_j^l) - I)^2, \quad (9)$$

where corr is a correlation matrix, F_i^l are the features of the i 'th generator at layer l and I is the identity matrix. Although this loss is not mandatory, we noticed it reduces overall correlation of ψ 's and emphasizes unique characteristics in each component.

The total loss is a weighted sum of the mentioned losses, in addition to the standard adversarial loss of GAN architecture [8]. Inference is performed by providing an image x and a class y (the inference diagram and additional training and inference details are in the supplementary).

Method	Datasets				
	Peppers	AFHQ	CelebA	BraTS	DOTA
Ours	0.542	0.754	0.651	0.649	0.608
LRP [5]	0.971	0.999	0.999	0.997	0.963
IG [30]	0.881	0.908	0.946	0.934	0.828
G-SH [19]	0.87	0.907	0.947	0.935	0.831
I-Inf. [21]	0.865	0.995	0.996	0.928	0.844
GGC [29]	1.0	1.0	1.0	0.999	0.981
GC [29]	0.966	1.0	0.999	0.996	0.901
Random	0.914	0.993	0.891	0.891	0.881

Table 1. AUC of the curve: classification accuracy of x_β as a function of β , see Eq. (10), with β ranging from 0 to 1. Lower AUC is better. See full explanation in Sec. 4.

4. Experiments

We show here various experiments examining the validity of our algorithm and the applicability of using the proposed method to infer useful classification explanations for various diverse data sets. Unless noted otherwise, we use ResNet18 [16] as our image classifier. The classification problem is

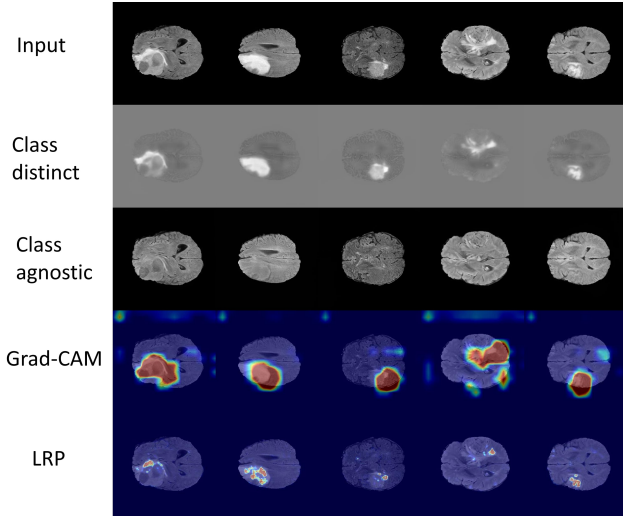


Figure 8. BraTS [25]: Tumors in MRI images, class-distinct and class-agnostic parts. The dataset included two classes, with and without tumors.

Ours	LRP	IG	G-SH	II	GGC	GC
0.125	0.156	0.171	0.172	0.177	0.179	0.192

Table 2. AUC comparison of the Faithfulness index on the BraTS dataset among various XAI methods. Ours is compared to LRP, Integrated gradients, Gradient SHAP, Internal influence, Guided Grad-Cam and Grad-Cam. AUC values were calculated based on the deletion of pixels, with up to 20% removed. When our CD part may be interpreted as importance (by pixel amplitude) one can validate our accurate XAI mapping also by standard evaluation methods.

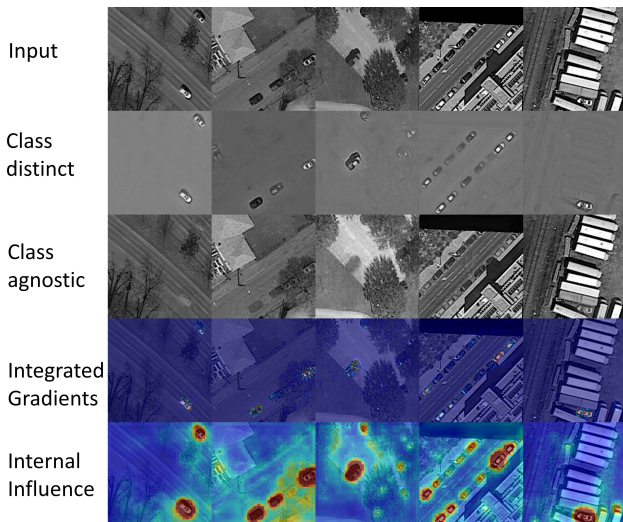


Figure 9. Cars (DOTA [34]): Class-distinct and Class-agnostic parts. The dataset included two classes, images with and without cars.

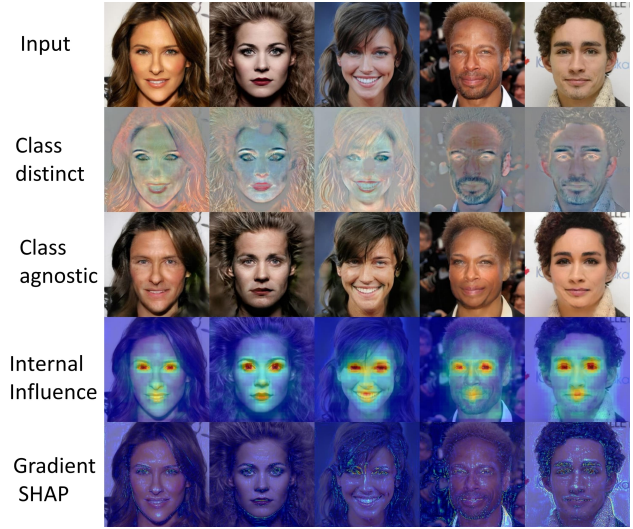


Figure 10. CeleBA [15]: Class-distinct and Class-agnostic parts. The dataset included male and female classes.

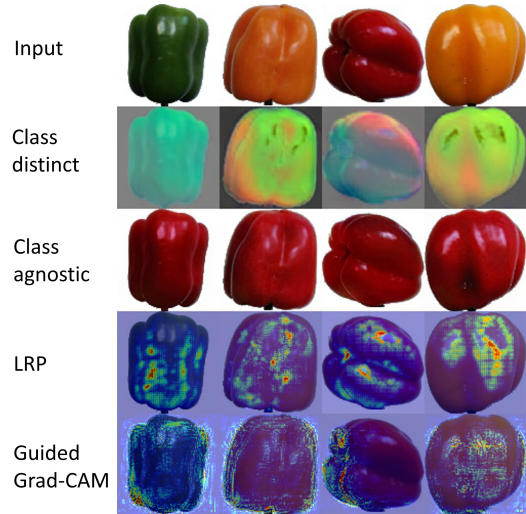


Figure 11. Peppers [31]: Class-distinct and Class-agnostic parts. The dataset included four classes of different colored peppers.

solved sufficiently well in all cases with about 95% or higher test accuracy.

In Fig. 7 we show a linear progression from the original image to the agnostic part by generating the images,

$$x_\beta = x - \beta \cdot \psi_{Distinct}, \quad (10)$$

where $\beta \in \{0, 0.25, 0.5, 0.75, 1\}$. For $\beta = 0$ we have the original image and for $\beta = 1$ the agnostic part. The average probability vector $p(x_\beta)$ is depicted, averaged for each class. A single image for each class is shown, illustrating this progression. We see class distinction diminishes. Note we do not obtain precise agnostic images for $\beta = 1$ but only an approximation.

	DOTA (cars)		AFHQ		Celeb A	
AUC according to:	ResNet18	Simple	ResNet18	Simple	ResNet18	Simple
Trained by ResNet18	0.793	0.903	0.737	0.759	0.616	0.707
Trained by Simple-Classifier	0.914	0.729	0.865	0.623	0.69	0.609

Table 3. **Matching explanation to classifier.** At each row DXAI training is performed using a different classifier. AUC (similar to Tab. 1) is shown, computed using the two classifiers, on three different data sets. AUC is smaller (better) when the classifier in training and the one used to compute the AUC match. This shows the relevance of the DXAI explanations to the classifier.

In Table 1 we show the results of a quantitative experiment comparing our method to other possible XAI decompositions. In this experiment we follow Eq. (10) for β ranging from 0 to 1 in increments of 0.1. As β grows accuracy should drop. We check the area under the curve (AUC) of accuracy vs. β , where lower AUC is better. More details appear in the supplementary. Since, as far as we know, we are the first to propose DXAI, we obtain a decomposition based on established XAI algorithms, implemented using Captum library [19]. One can produce a decomposition from a heatmap $H \geq 0$ by a normalization, having a weight for each pixel, $w = \frac{H}{\max(H)} \in [0, 1]$, and defining for an image x , $\psi_{Distinct} := w \cdot x$, $\psi_{Agnostic} := (1 - w) \cdot x$. We get a decomposition in the form of Eq. (1), such that $x = \psi_{Distinct} + \psi_{Agnostic}$, see examples in Fig. 4. Table 1 demonstrates that for all data sets our decomposition outperforms all other methods by a considerable margin. This indicates our proposed method has evidently different qualitative properties, such that trivial manipulations of the heatmap cannot generate high quality class-distinct components.

Our algorithm does not provide importance ranking of each pixels, with respect to its contribution for the classification. This is one of its limitations. Thus we cannot use the standard way to evaluate XAI accuracy by removing pixels gradually based on importance, as done e.g. in [28]. In some problems, however, a simple ranking can be inferred by our algorithm. In a binary classification problem, when one class is predominantly decided based on the existence of certain lighter pixels, we can use the amplitude of pixels in $\psi_{Distinct}$ as a reasonable importance ranking. In this case standard XAI evaluation can be made. The BraTS dataset [25] is such a case. It contains MRI scans of the human brain used for brain tumor segmentation research. The dataset includes scans from patients with brain tumors, along with expert annotations for tumor regions. In many cases, bright regions indicate evidence of tumors. We divided the dataset into two classes: images containing tumors and images that do not. Some example results are shown in Fig. 8. Table 2 shows the standard AUC evaluation on this set (AUC of accuracy vs. number of pixels removed, ordered by importance). We see our algorithm behaves favorably both qualitatively and quantitatively.

An XAI algorithm should naturally depend on the specific classifier C at hand. Different classifiers may yield different

class distinct and class agnostic parts. We check this is indeed the case in Table 3. We compare our results when C is ResNet18 and when C is a simpler classifier with fewer layers, referred to as ‘‘Simple’’ (yielding less accurate results, details in the supplementary). We compare AUC as done for Tab. 1. Here however, the accuracy graph is computed twice - using each of the above classifiers. We show AUC drops more sharply when C used for obtaining $\psi_{Distinct}$ in Eq. (10) matches the classifier for computing the AUC. The experiment demonstrates that our map effectively captures the characteristics of the target classifier.

In Figs. 9, 10 and 11 we show additional examples for various datasets. In general, our method is especially effective in cases where the differences between the classes have an additive nature. This occurs in situations where the differences involve textures (head- and facial-hair in Fig. 10), colors (Fig. 11), and the presence or absence of details, such as cars (Fig. 9), red lips or heavy eyebrows (Fig. 10).

5. Discussion and Conclusion

We propose an alternative way to analyze and to visualize the reasons for classification by neural networks. It is based on decomposing the image into a part which does not contribute to the classification and to one which holds the class-related cues. This approach may not be ideal for all applications and has several *limitations and drawbacks*, compared to standard XAI methods: 1. The method requires training, for a specific training set and classifier (training is slow, inference is fast); 2. There is no natural ranking of the significance of pixels in the image. The amplitude of pixels in the class-distinct part can serve as a good approximation; 3. Our implementation uses GANs. We note that image realism is of secondary significance for XAI. Our concept does not rely on a GAN architecture and improvements may be achieved by diffusion-type generative models, such as [7, 17, 33, 36].

Major advantages afforded by this method are of obtaining detailed, dense, high-resolution, multi-channel information for class distinction. We propose, for the first time, a decomposition problem for XAI purposes, allowing to clearly visualize also image components which are not relevant for the classification task (agnostic part). We examine and compare our method in the context of several classification tasks and data sets, showing the applicability and additional insights afforded by this new approach.

References

- [1] Michal Aharon, Michael Elad, and Alfred Bruckstein. K-svd: An algorithm for designing overcomplete dictionaries for sparse representation. *IEEE Transactions on signal processing*, 54(11):4311–4322, 2006. [2](#)
- [2] Gulsum Alicioglu and Bo Sun. A survey of visual analytics for explainable artificial intelligence methods. *Computers & Graphics*, 102:502–520, 2022. [1](#)
- [3] Jean-François Aujol and Antonin Chambolle. Dual norms and image decomposition models. *International journal of computer vision*, 63:85–104, 2005. [2](#)
- [4] Jean-François Aujol, Guy Gilboa, Tony Chan, and Stanley Osher. Structure-texture image decomposition—modeling, algorithms, and parameter selection. *International journal of computer vision*, 67:111–136, 2006. [2](#)
- [5] Alexander Binder, Grégoire Montavon, Sebastian Lapuschkin, Klaus-Robert Müller, and Wojciech Samek. Layer-wise relevance propagation for neural networks with local renormalization layers. In *Artificial Neural Networks and Machine Learning–ICANN 2016: 25th International Conference on Artificial Neural Networks, Barcelona, Spain, September 6-9, 2016, Proceedings, Part II 25*, pages 63–71. Springer, 2016. [2](#), [6](#)
- [6] Jonathan Brokman and Guy Gilboa. Analysis of branch specialization and its application in image decomposition. *arXiv preprint arXiv:2206.05810*, 2022. [3](#), [5](#)
- [7] Jingwen Chen, Yingwei Pan, Ting Yao, and Tao Mei. Control-style: Text-driven stylized image generation using diffusion priors. In *Proceedings of the 31st ACM International Conference on Multimedia*, pages 7540–7548, 2023. [8](#)
- [8] Yunjey Choi, Youngjung Uh, Jaejun Yoo, and Jung-Woo Ha. Stargan v2: Diverse image synthesis for multiple domains. In *Proceedings of the IEEE Conference on Computer Vision and Pattern Recognition*, 2020. [1](#), [3](#), [6](#), [11](#), [12](#)
- [9] Ingrid Daubechies. *Ten lectures on wavelets*. SIAM, 1992. [2](#)
- [10] David L Donoho, Michael Elad, and Vladimir N Temlyakov. Stable recovery of sparse overcomplete representations in the presence of noise. *IEEE Transactions on information theory*, 52(1):6–18, 2005. [2](#)
- [11] Rudresh Dwivedi, Devam Dave, Het Naik, Smiti Singhal, Rana Omer, Pankesh Patel, Bin Qian, Zhenyu Wen, Tejal Shah, Graham Morgan, et al. Explainable ai (xai): Core ideas, techniques, and solutions. *ACM Computing Surveys*, 55(9): 1–33, 2023. [1](#)
- [12] M Jalal Fadili, Jean-Luc Starck, Jérôme Bobin, and Yassir Moudden. Image decomposition and separation using sparse representations: An overview. *Proceedings of the IEEE*, 98(6):983–994, 2009. [2](#)
- [13] Marzyeh Ghassemi, Luke Oakden-Rayner, and Andrew L Beam. The false hope of current approaches to explainable artificial intelligence in health care. *The Lancet Digital Health*, 3(11):e745–e750, 2021. [1](#)
- [14] Ioanna Gkartzonika, Nikolaos Gkalelis, and Vasileios Mezaris. Learning visual explanations for dcnn-based image classifiers using an attention mechanism. In *European Conference on Computer Vision*, pages 396–411. Springer, 2022. [2](#)
- [15] Yandong Guo, Lei Zhang, Yuxiao Hu, Xiaodong He, and Jianfeng Gao. Ms-celeb-1m: A dataset and benchmark for large-scale face recognition. In *Computer Vision–ECCV 2016: 14th European Conference, Amsterdam, The Netherlands, October 11-14, 2016, Proceedings, Part III 14*, pages 87–102. Springer, 2016. [7](#), [11](#)
- [16] Kaiming He, Xiangyu Zhang, Shaoqing Ren, and Jian Sun. Deep residual learning for image recognition. In *Proceedings of the IEEE conference on computer vision and pattern recognition*, pages 770–778, 2016. [6](#)
- [17] Guillaume Jeanneret, Loïc Simon, and Frédéric Jurie. Diffusion models for counterfactual explanations. In *Proceedings of the Asian Conference on Computer Vision*, pages 858–876, 2022. [3](#), [8](#)
- [18] Vidhya Kamakshi and Narayanan C Krishnan. Explainable image classification: The journey so far and the road ahead. *AI*, 4(3):620–651, 2023. [1](#)
- [19] Narine Kokhlikyan, Vivek Miglani, Miguel Martin, Edward Wang, Bilal Alsallakh, Jonathan Reynolds, Alexander Melnikov, Natalia Kliushkina, Carlos Araya, Siqi Yan, and Orion Reblitz-Richardson. Captum: A unified and generic model interpretability library for pytorch, 2020. [6](#), [8](#)
- [20] Piotr Komorowski, Hubert Baniecki, and Przemyslaw Biecek. Towards evaluating explanations of vision transformers for medical imaging. In *Proceedings of the IEEE/CVF Conference on Computer Vision and Pattern Recognition*, pages 3725–3731, 2023. [2](#)
- [21] Klas Leino, Shayak Sen, Anupam Datta, Matt Fredrikson, and Linyi Li. Influence-directed explanations for deep convolutional networks. In *2018 IEEE international test conference (ITC)*, pages 1–8. IEEE, 2018. [6](#)
- [22] Scott M Lundberg and Su-In Lee. A unified approach to interpreting model predictions. *Advances in neural information processing systems*, 30, 2017. [2](#)
- [23] Stephane G Mallat. A theory for multiresolution signal decomposition: the wavelet representation. *IEEE transactions on pattern analysis and machine intelligence*, 11(7):674–693, 1989. [2](#)
- [24] Charles Marx, Youngsuk Park, Hilaf Hasson, Yuyang Wang, Stefano Ermon, and Luke Huan. But are you sure? an uncertainty-aware perspective on explainable ai. In *International Conference on Artificial Intelligence and Statistics*, pages 7375–7391. PMLR, 2023. [3](#)
- [25] Bjoern H Menze, Andras Jakab, Stefan Bauer, Jayashree Kalpathy-Cramer, Keyvan Farahani, Justin Kirby, Yuliya Burten, Nicole Porz, Johannes Slotboom, Roland Wiest, et al. The multimodal brain tumor image segmentation benchmark (brats). *IEEE transactions on medical imaging*, 34(10):1993–2024, 2014. [7](#), [8](#), [11](#), [12](#)
- [26] Silvan Mertes, Tobias Huber, Katharina Weitz, Alexander Heimerl, and Elisabeth André. Ganterfactual—counterfactual explanations for medical non-experts using generative adversarial learning. *Frontiers in artificial intelligence*, 5:825565, 2022. [3](#)
- [27] Marco Tulio Ribeiro, Sameer Singh, and Carlos Guestrin. “why should i trust you?” explaining the predictions of any classifier. In *Proceedings of the 22nd ACM SIGKDD interna-*

- tional conference on knowledge discovery and data mining*, pages 1135–1144, 2016. 2
- [28] Wojciech Samek, Alexander Binder, Grégoire Montavon, Sebastian Lapuschkin, and Klaus-Robert Müller. Evaluating the visualization of what a deep neural network has learned. *IEEE transactions on neural networks and learning systems*, 28(11):2660–2673, 2016. 8
- [29] Ramprasaath R Selvaraju, Michael Cogswell, Abhishek Das, Ramakrishna Vedantam, Devi Parikh, and Dhruv Batra. Grad-cam: Visual explanations from deep networks via gradient-based localization. In *Proceedings of the IEEE international conference on computer vision*, pages 618–626, 2017. 2, 6
- [30] Mukund Sundararajan, Ankur Taly, and Qiqi Yan. Axiomatic attribution for deep networks. In *International conference on machine learning*, pages 3319–3328. PMLR, 2017. 2, 6
- [31] Dang Thi Phuong Chung and Dinh Van Tai. A fruits recognition system based on a modern deep learning technique. In *Journal of physics: conference series*, page 012050. IOP Publishing, 2019. 7, 11, 12
- [32] Tom Vermeire, Dieter Brughmans, Sofie Goethals, Raphael Mazzine Barbossa de Oliveira, and David Martens. Explainable image classification with evidence counterfactual. *Pattern Analysis and Applications*, 25(2):315–335, 2022. 2
- [33] Zhizhong Wang, Lei Zhao, and Wei Xing. Stylediffusion: Controllable disentangled style transfer via diffusion models. In *Proceedings of the IEEE/CVF International Conference on Computer Vision*, pages 7677–7689, 2023. 8
- [34] Gui-Song Xia, Xiang Bai, Jian Ding, Zhen Zhu, Serge Belongie, Jiebo Luo, Mihai Datcu, Marcello Pelillo, and Liangpei Zhang. Dots: A large-scale dataset for object detection in aerial images. In *Proceedings of the IEEE conference on computer vision and pattern recognition*, pages 3974–3983, 2018. 7, 11, 12
- [35] Mengqi Xue, Qihan Huang, Haofei Zhang, Lechao Cheng, Jie Song, Minghui Wu, and Mingli Song. Protopformer: Concentrating on prototypical parts in vision transformers for interpretable image recognition. *arXiv preprint arXiv:2208.10431*, 2022. 2
- [36] Serin Yang, Hyunmin Hwang, and Jong Chul Ye. Zero-shot contrastive loss for text-guided diffusion image style transfer. *arXiv preprint arXiv:2303.08622*, 2023. 8
- [37] Xiaoge Zhang, Felix TS Chan, and Sankaran Mahadevan. Explainable machine learning in image classification models: An uncertainty quantification perspective. *Knowledge-Based Systems*, 243:108418, 2022. 3

A. Detailed description of the method

A.1. Training

In the main paper, we presented the training method and primary loss functions. However, for brevity, we omitted details on functions that are neither innovative nor crucial for understanding the method’s general concept. Additionally, these functions serve similar purposes to those already discussed.

One such function, integral to the GAN architecture implementation but not explicitly mentioned, is the adversarial loss as defined in [8]

$$L_{adv} = \mathbb{E}_{x,y} [\log D_y(x^y)] + \mathbb{E}_{x,\hat{y}} [\log(1 - D_{\hat{y}}(\hat{x}^{\hat{y}}))], \quad (11)$$

where D_y represents the y ’th element of a vector of length c , which is an output of the discriminator. Its role is to ensure that the generators produce images resembling real ones, for a given class.

Another function, briefly mentioned, directs our discriminator not only to classify images but also to align with the classifications of our trained classifier. This encourages the discriminator to assign a high score only to the correct class according to the classifier

$$L_{KLD} = KLD(D(x^y), C(x^y)), \quad (12)$$

where KLD is the Kullback-Leibler distance.

In addition to the reconstruction loss explained in the main part, one can use additional constraints on the reconstruction to enhance results. Specifically, we observed challenges in reproducing areas with significant differences between classes. To address this, we incorporated an additional constraint for reconstruction between pixels with a high amplitude in the distinction branch. High amplitude signifies differences between classes due to the additive nature of the model. We remind that we use the following distance measure

$$d(u, v) = \|u - v\|_{L^1} + \|u - v\|_{L^2},$$

with a reconstruction loss of the form

$$L_{rec} = d(x, \hat{x}^y) + d(x, \hat{x}^{\hat{y}}).$$

The proposed loss function is

$$L_{dis-rec} = d(x \odot \mathbb{I}, \hat{x}^y \odot \mathbb{I}), \quad (13)$$

where

$$\mathbb{I} = \begin{cases} 1 & \text{if } |\psi_1^y| > \text{mean}(|\psi_1^y|) \\ 0 & \text{else,} \end{cases}$$

and \odot denotes element-wise product.

The full objective loss is:

$$L_{Total} = \lambda_{adv} L_{adv} + \lambda_{KLD} L_{KLD} + \lambda_{cf} L_{class-fake} + \lambda_{rec} L_{rec} + \lambda_{dr} L_{dis-rec} + \lambda_o L_{orth}. \quad (14)$$

In our experiments we used the following weights:

$$\lambda_{adv} = 2, \lambda_{KLD} = 1, \lambda_{cf} = 2, \lambda_{rec} = 4, \lambda_{dr} = 4, \lambda_o = 1. \quad (15)$$

A note on how weights can be adjusted. The rule of thumb is that for applications where particularly good reconstruction is required, the weights for reconstruction should be increased. Conversely, when style transition is challenging and there are more hidden characteristics, the weights for classification and adversarial loss should be increased.

A.2. Inference Stage

The inference stage is described in Fig. 12. The input x^y is an image x of class y . The class predicted by the classifier is \hat{y} . We would like to explain the classification result by the trained DXAI model. The class distinct part is given by the first generator. The rest of the summed branches provide the agnostic part.

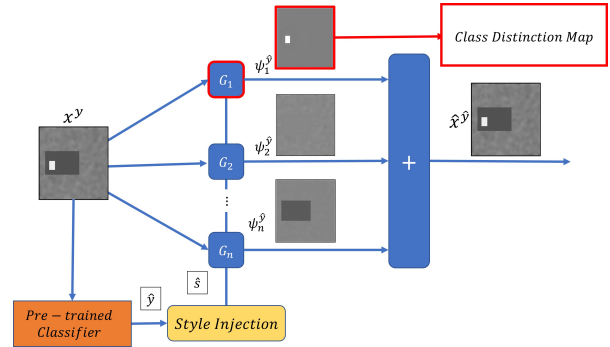


Figure 12. Inference stage: the input image and the predicted class are used to guide the generators. The output is comprised of the class distinction map in the first branch and the agnostic part by a sum of the rest of the branches.

Datasets	Train set	Test set
AFHQ [8]	14630	1500
CelebA [15]	28000	2000
DOTA(cars) [34]	172465	20696
BraTS [25]	15000	1232
Peppers [31]	2478	826
Tomatoes [31]	5103	1707
Apples [31]	6404	2134

Table 4. Number of images in each dataset.

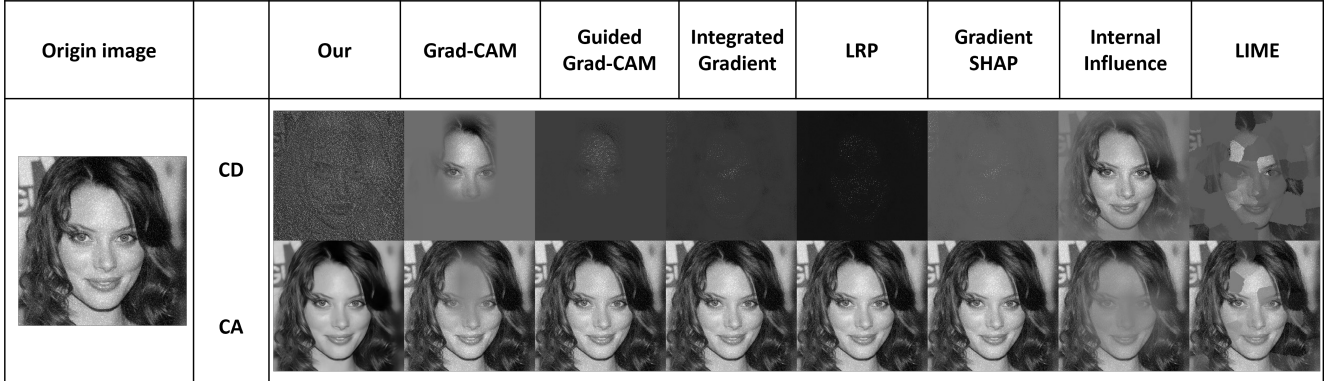


Figure 13. **Noise distinction.** Celeb-A where one class contains clean images and the other class contains noisy images, contaminated by additive white Gaussian noise (AWGN). In this case, standard XAI algorithms yield partial and inaccurate explanation of the class distinction. Our algorithm provides a correct explanation distinguishing the two classes by isolating well the noise.

Datasets	ResNet18	Simple	Discriminator
AFHQ	0.975	0.906	0.994
CelebA	0.978	0.96	0.988
DOTA(cars)	0.863	0.749	0.858
BraTS	0.912	0.877	0.982
Peppers	1	0.944	1
Tomatoes	1	0.985	1
Apples	0.983	0.909	1

Table 5. Test accuracy of each classifier.

Simple-Classifier Architecture	Dimension
Input image	256x256x3
Conv2d(3, 16, 3x3)	256x256x16
MaxPool2d(3x3)	85x85x16
ReLU	
Conv2d(16, 32, 3x3)	85x85x32
MaxPool2d(3x3)	28x28x32
Linear(in=28*28*32, out=128)	128
ReLU	
Linear(in=128, out=c)	c

Table 6. Simple-Classifier Architecture from input to output. c is the number of classes and input image can be also a gray scale image.

A.3. Datasets

In the main paper several datasets were used. We provide some more technical details on those sets. In Tab. 4 the number of images of each set is given. Some datasets were adjusted or filtered to suit the classification task. For instance, in the case of DOTA [34], which contains high-resolution aerial images with objects marked in bounding boxes, we divided the images into patches of size 256x256 pixels and categorized them into two classes. One class comprised images

Discriminator Architecture	Dimension
Input image	256x256x3
Conv1x1	256x256x64
ResBlk	128x128x128
ResBlk	64x64x256
ResBlk	32x32x512
ResBlk	16x16x512
ResBlk	8x8x512
ResBlk	4x4x512
Leaky-ReLU	
Conv4x4	1x1x512
Leaky-ReLU	
Conv1x1	c

Table 7. Discriminator Architecture as given in [8] from input to output. c is the number of classes and unlike the original architecture the input image can be also a gray scale image.

featuring at least 70% of a single car (in many cases there are multiple cars), while the other class included images with no cars at all. The classifier was trained to distinguish between these two classes of patches. As expected, the explanation (distinct) image is comprised of isolated cars.

To identify fruits, we employed the Fruits 360 dataset [31]. From there, we selected specific classes of peppers, tomatoes, and apples, which mainly differ in color and texture, and created a dataset for each.

For BraTS [25], we only considered a subset of the images—specifically, those in which the tumor occupied an area of at least 20 pixels were included in the class designated to contain tumors. Images that did not contain a tumor at all but featured a full cross-section of the brain were included in the second class. Subsequently, we randomly split the images into train and test sets.

No modifications were made to the remaining datasets.



Figure 14. AFHQ ablation - need of more than 2 branches. The run of the experiment was stopped after 150K iterations, after the tendency was understood.

A.4. Classifiers

In our experiments three different classifiers were employed for the classification block C : a ResNet18-type classifier, a simple classifier described in Tab. 6, and our discriminator D , which possesses classification capabilities, as the output is a vector of length c , indicating class probabilities (details of the architecture are in Tab. 7). The test accuracy of each classifier is given in Tab. 5. We note that the discriminator exhibits the best classification performance. Thus, we selected it in the main paper to show the explanation images by the various DXAI and XAI algorithms. Note that we found a mistake in the explanation text of the paper, which will be corrected in the final version. We conducted experiments also on ResNet18 and on the Simple classifier, showing consistently similar trends. We provide later some examples of ResNet18 results on the same datasets.

The intentionally designed simple classifier, with lower classification ability, provides distinct classification results from a well-known classifier like ResNet18. This intentional dissimilarity allows for meaningful comparisons of their results, as detailed in the main paper.

B. Ablation

In the ablation study, we investigated two key factors. Firstly, we examined the impact of the number of branches. While decomposing the classified image into several images, we primarily focus on solving only two images—distinct and agnostic. One might question why not use only two branches for the solution, since two branches can be trained to achieve a similar solution.

We show that when branches are used for the agnostic part results are better both in terms of reconstruction and of the generators’ ability to produce images that explain the classi-

fier. For instance, as demonstrated in Figs. 14 and 15, PSNR decreases when using only two branches. Additionally, the loss $L_{class-fake}$, representing the generators’ ability to produce meaningful images of a specific class according to the given classifier, is higher for the entire training with two branches. In other words, the classifier interprets the images less accurately as the desired class, making the images less reliable. The additional generators provide better generation capacity and can be trained in an easier and more stable manner.

In addition, we evaluated the impact of the loss $L_{dis-rec}$ described in Eq. (13) on the reconstruction quality. As explained earlier, we employed it because we observed that reconstruction, especially in areas with differences between the classes, was challenging. We conducted experiments both with and without it. We show that it indeed contributes to the quality of the reconstruction in terms of PSNR, as illustrated in Fig. 16.

It should be noted that, due to time constraints, we did not run the ablation experiments until the convergence of an optimal solution. Instead, we stopped the training after observing a discernible trend in the change of solution quality.

C. More results

In the main paper we presented qualitative results of our algorithm for different datasets with selected comparisons to other methods. Here we provide more detail. We show for each image the full comparison to 6 established XAI methods. We also provide more examples in each dataset, so the reader can judge better the quality and stability of our algorithm. We show the results for the case $C = D$ where the classifier is the discriminator (where classification accuracy is best) and for $C = ResNet18$, cases which

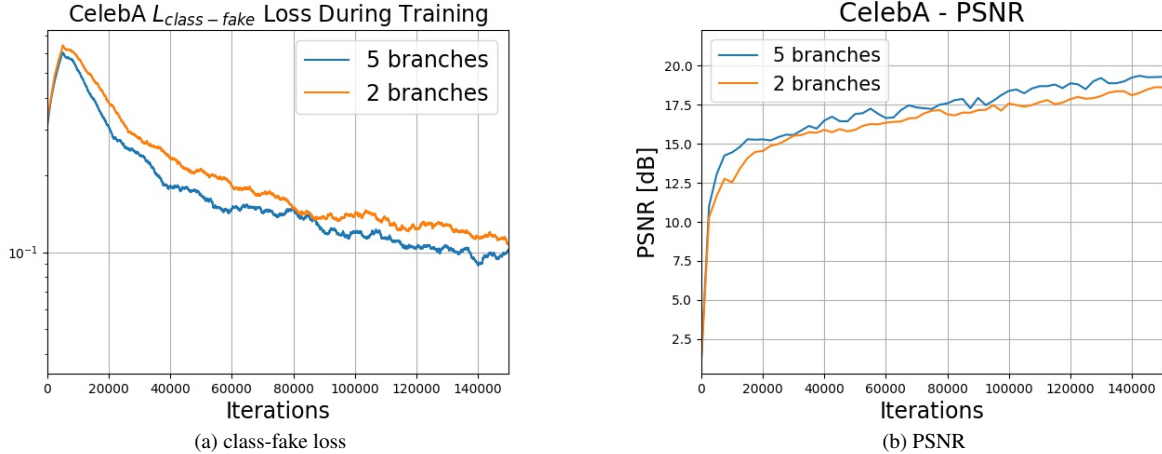


Figure 15. CelebA ablation - need of more than 2 branches. The run of the experiment was stopped after 150K iterations, after the tendency was understood.

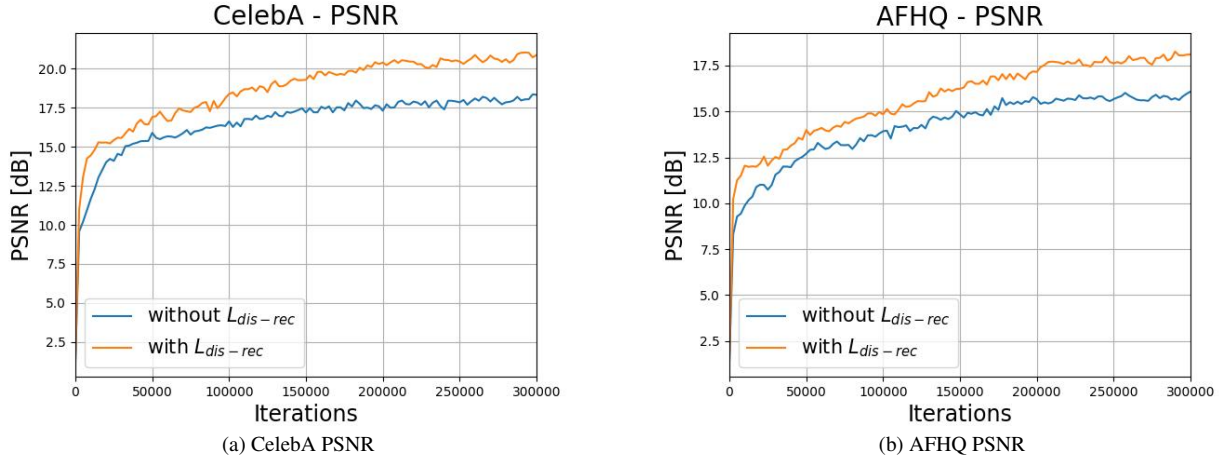


Figure 16. Ablation of $L_{dis-rec}$, it can be seen that without this loss function the PSNR is reduced

were not shown in the main paper. In Fig. 17 we show comparison between Female and Male classes. There are many subtle cues for such distinction. One can observe that our method provides dense informative explanations which highlight well the distinctions. In Fig. 18 the peppers are shown, which differ mainly by color, as our proposed method shows clearly. Heatmap visualization cannot show well global color explanations. In Fig. 19 we show that the cars are well isolated in high resolution by our method. This case is less dense and can be handled well also by some other methods (such as LRP, Guided grad-cam or Gradient SHAP). Our method appears to visualize the explanation very clearly. In Fig. 20 and Fig. 21 we show additional datasets of tomatoes and apples classes, which did not appear in the main paper. Here again color changes are a main feature of distinction, which is shown clearly by our method. In Fig. 22 additional

examples of the BraTS dataset are provided, showing our ability to isolate the lesions well. In Fig. 23 we observe the dense distinction images of animal classes, where different fur textures are significant features. These are very hard to visualize by heatmaps. The above images were using the discriminator as the classifier. In Fig. 24, Fig. 25, Fig. 26 and Fig. 27 we show results for ResNet18 as the classifier. We can expect that since both classifiers are relatively advanced, with high precision, they consider similar features. We can observe that our method produce qualitatively quite similar results and is stable. For the peppers case, Fig. 27, we observe a stronger difference, where the agnostic part is more of a mix of orange and red colors. In any case, the color distinction is clear and is much better visualized than in standard XAI methods. In Figs 28, 29, 30, 31 the classification explanations for the Simple classifier are shown. One

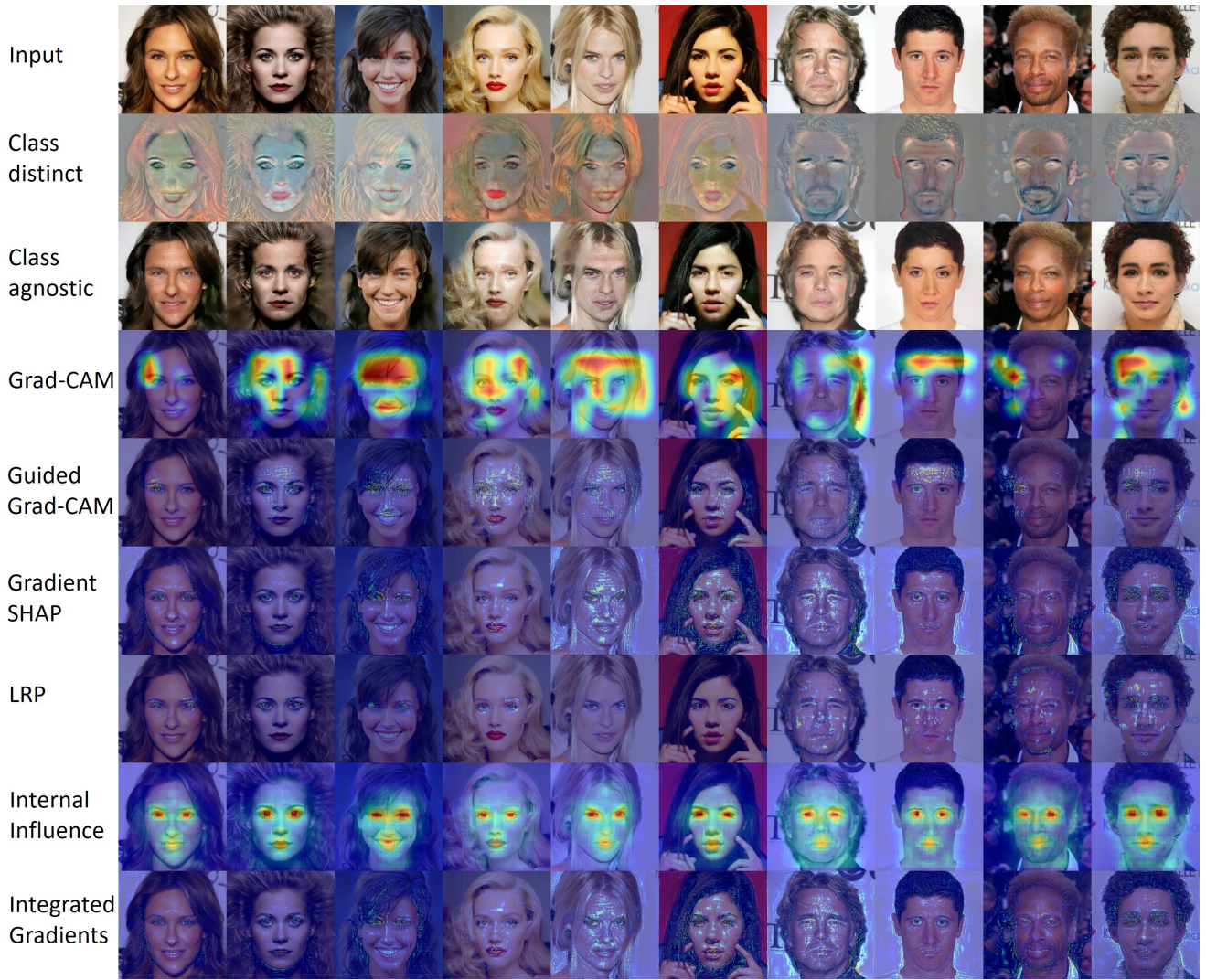


Figure 17. CelebA (Female and Male classes, $C = D$). The class distinct part shows for Female distinction by red lips, hair texture, eye-lashes and eyebrows. Fro Male – facial hair, heavy eyebrows, strong chin and visibility of ears. Other XAI algorithms capture only parts of the full explanation for such a complex classification task, which involves many subtle cues.

can observe that the distinction map is less accurate, more blurry, containing some spurious background features. This can be expected for a lower quality classifier.

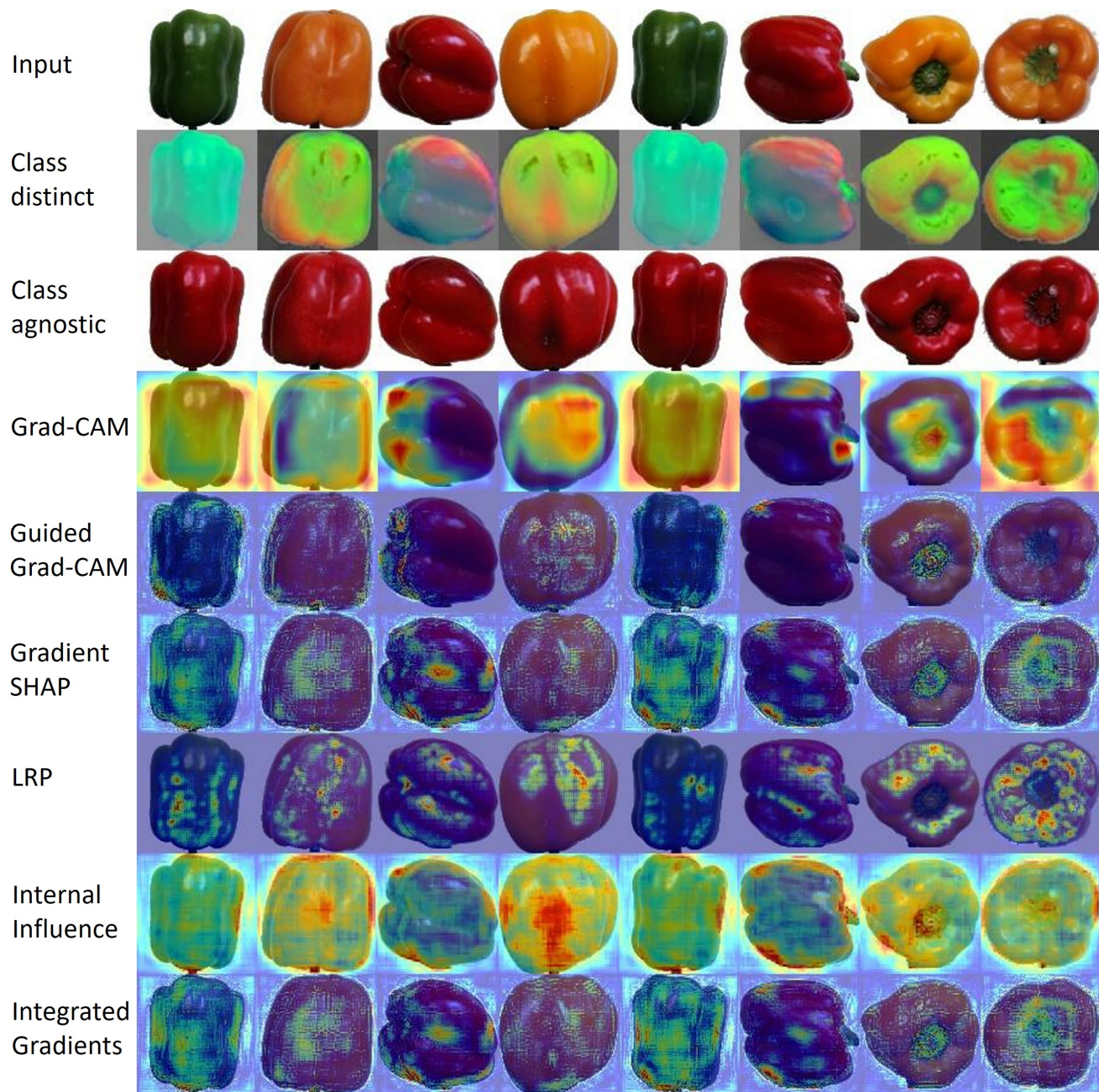


Figure 18. Peppers dataset ($C = D$). Class distinction is mainly by color, which is well visualized by our explanation method.

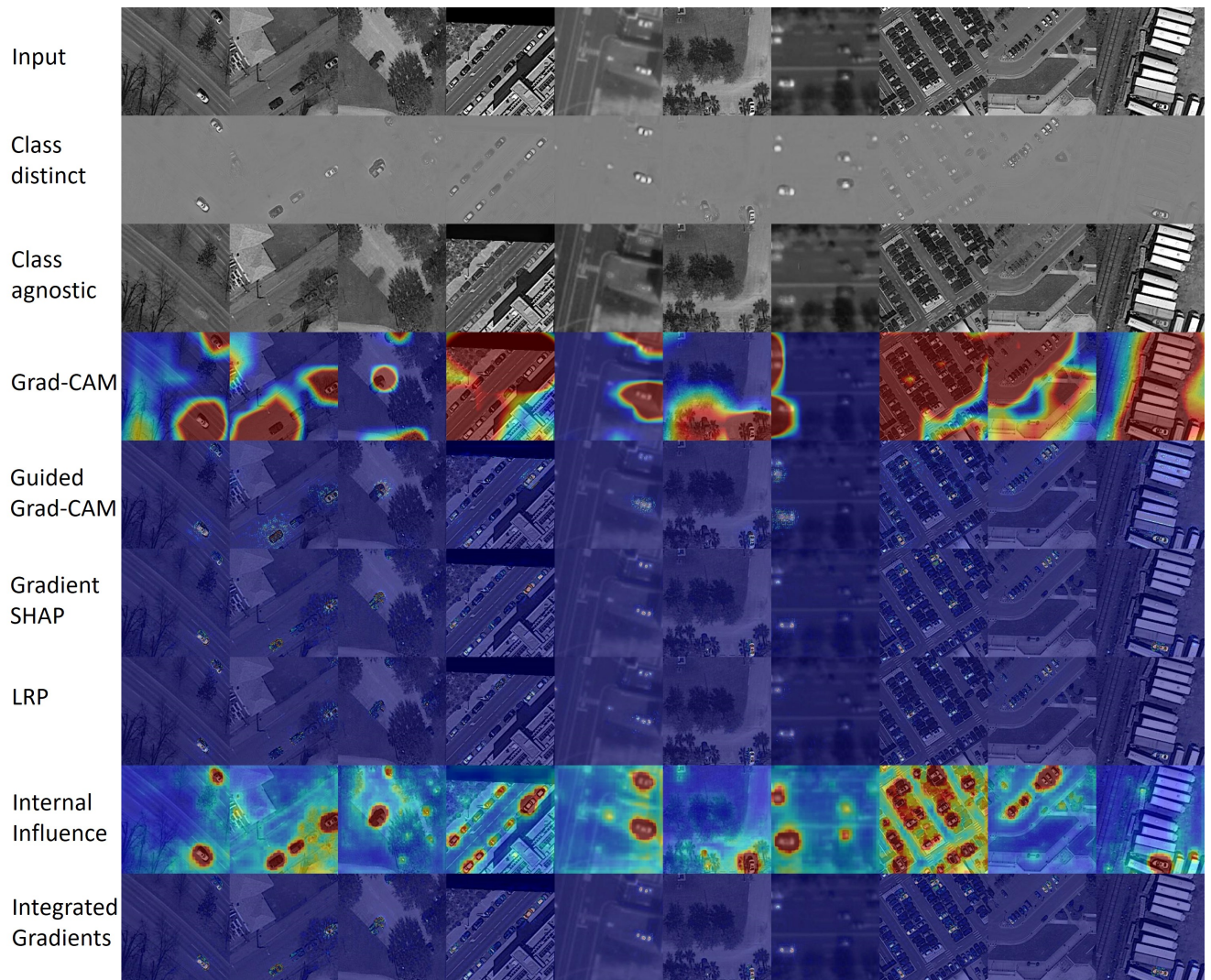


Figure 19. DOTA (cars) dataset ($C = D$). Cars are isolated well in the distinction part.

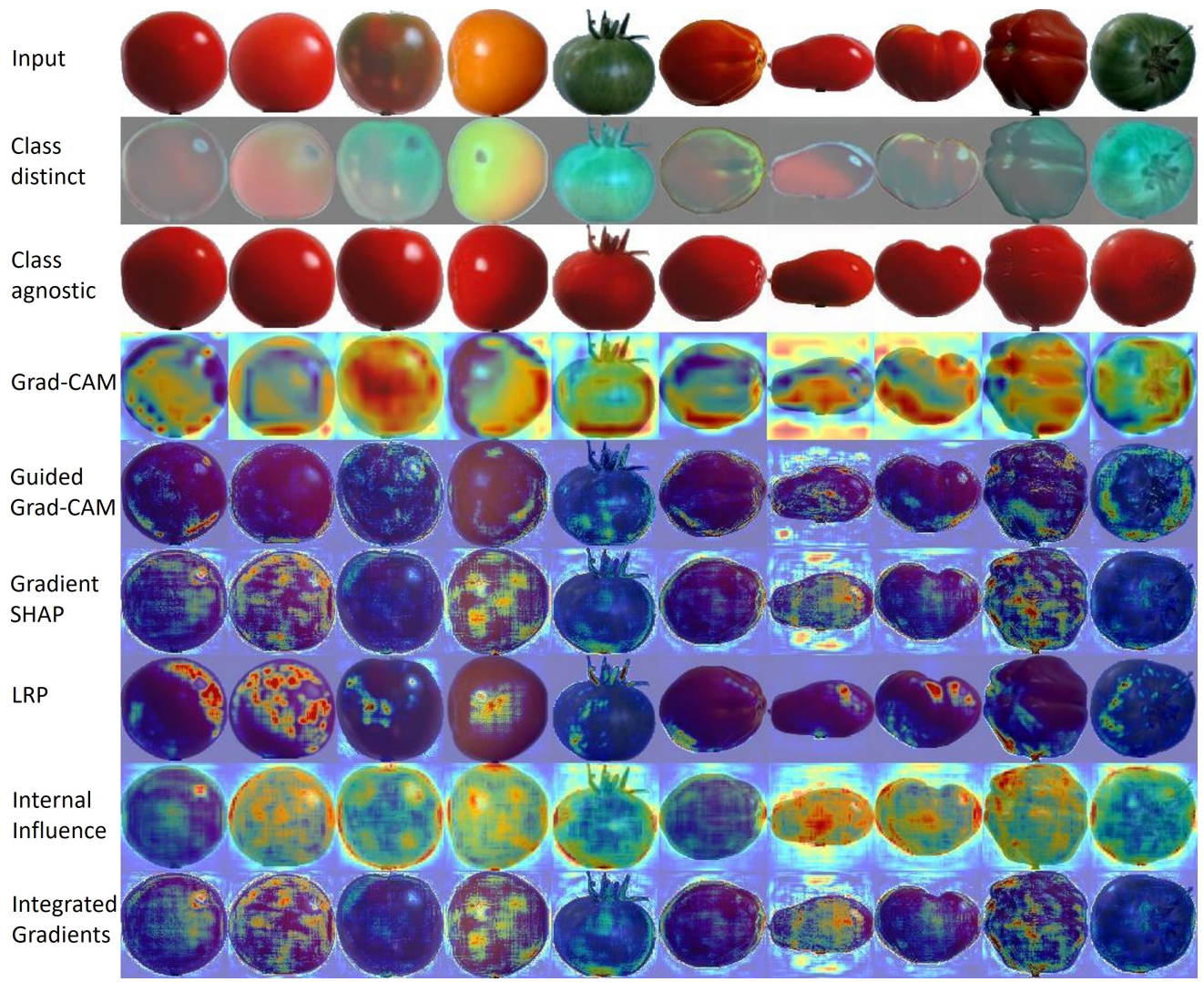


Figure 20. Tomatoes dataset ($C = D$). Distinction is mostly based on color (and some global texture).

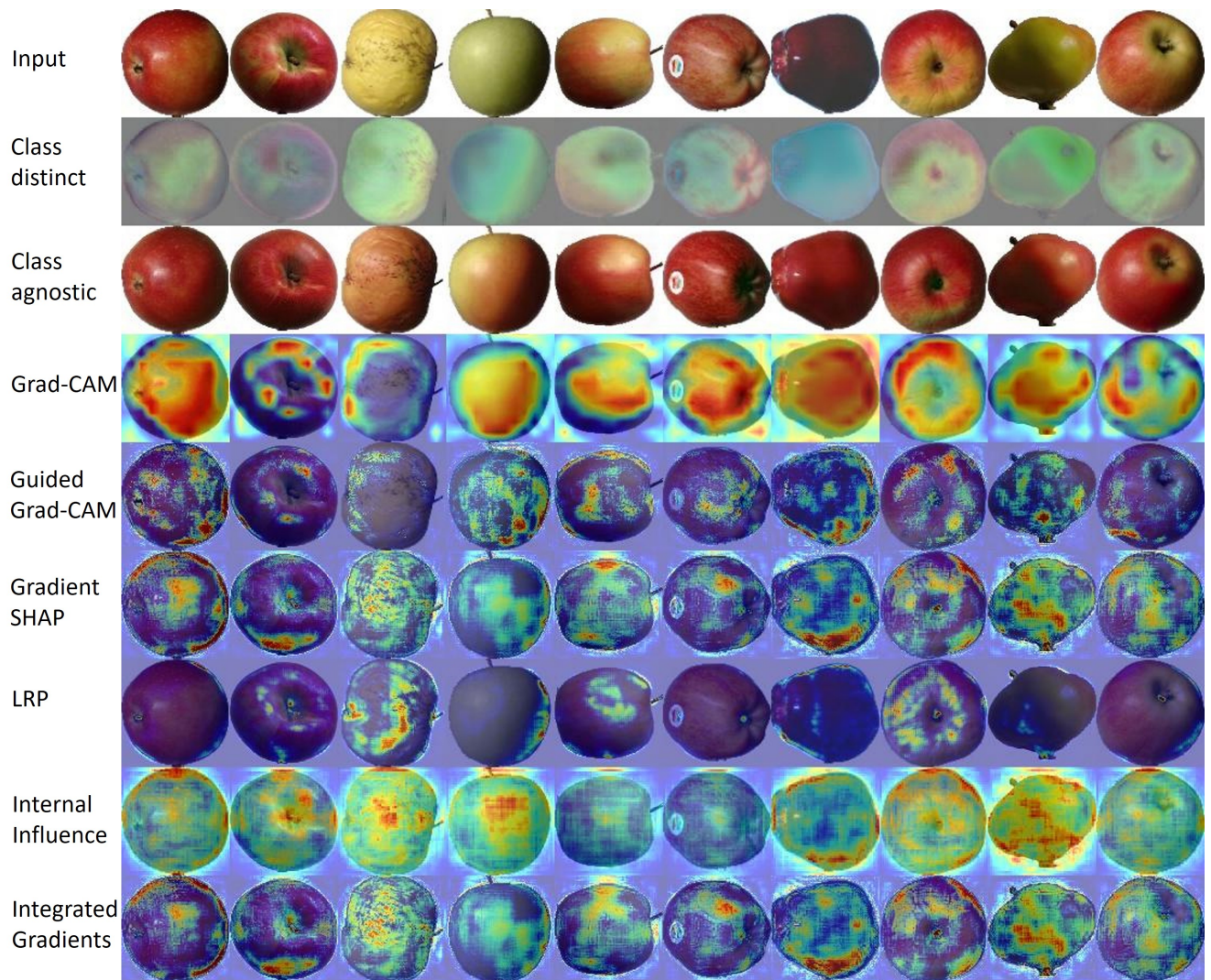


Figure 21. Apples dataset ($C = D$). Distinction by color is well captured by our methods.

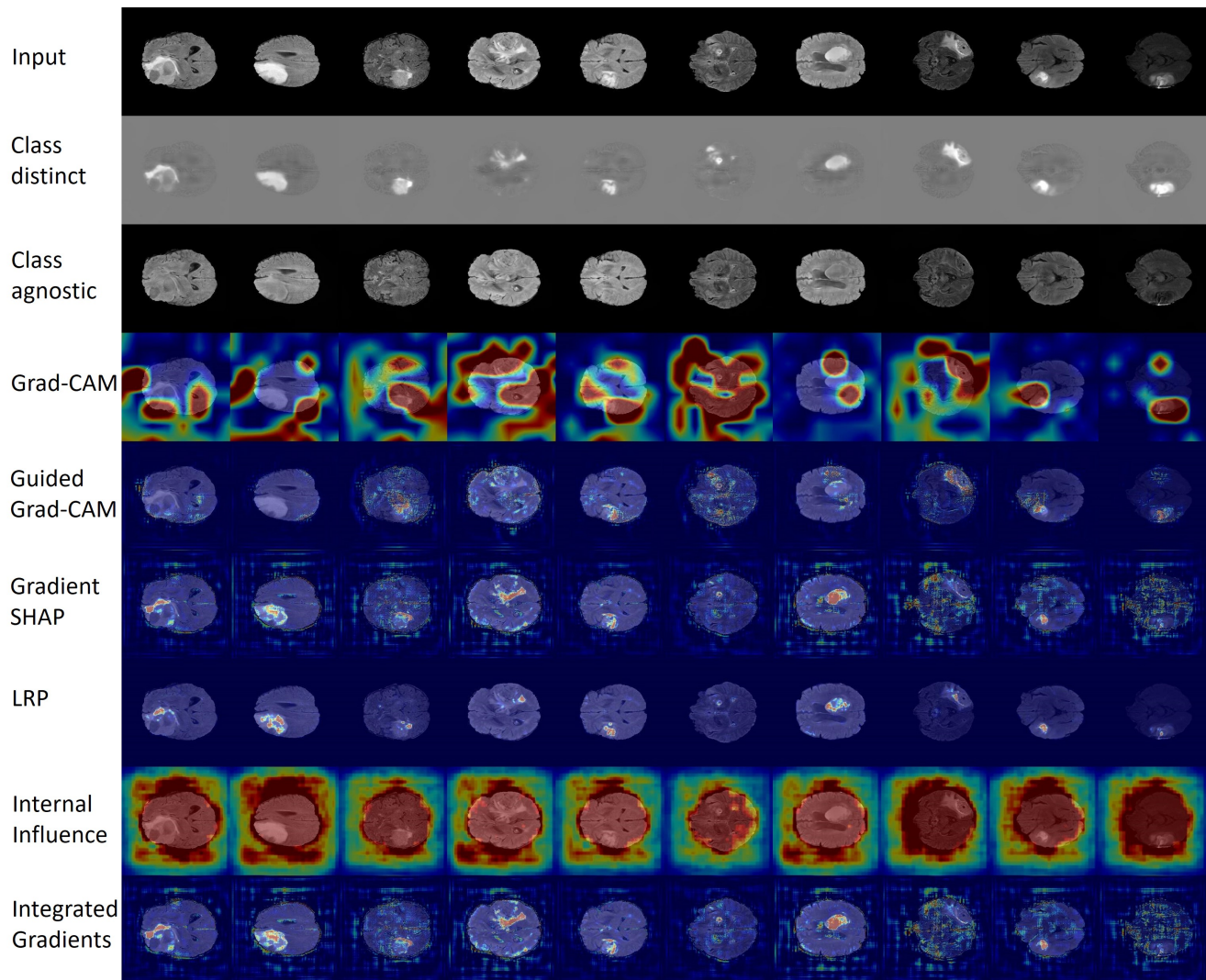


Figure 22. BraTS dataset ($C = D$). Highly localized regions of the lesions are visualized well in high resolution by our method.

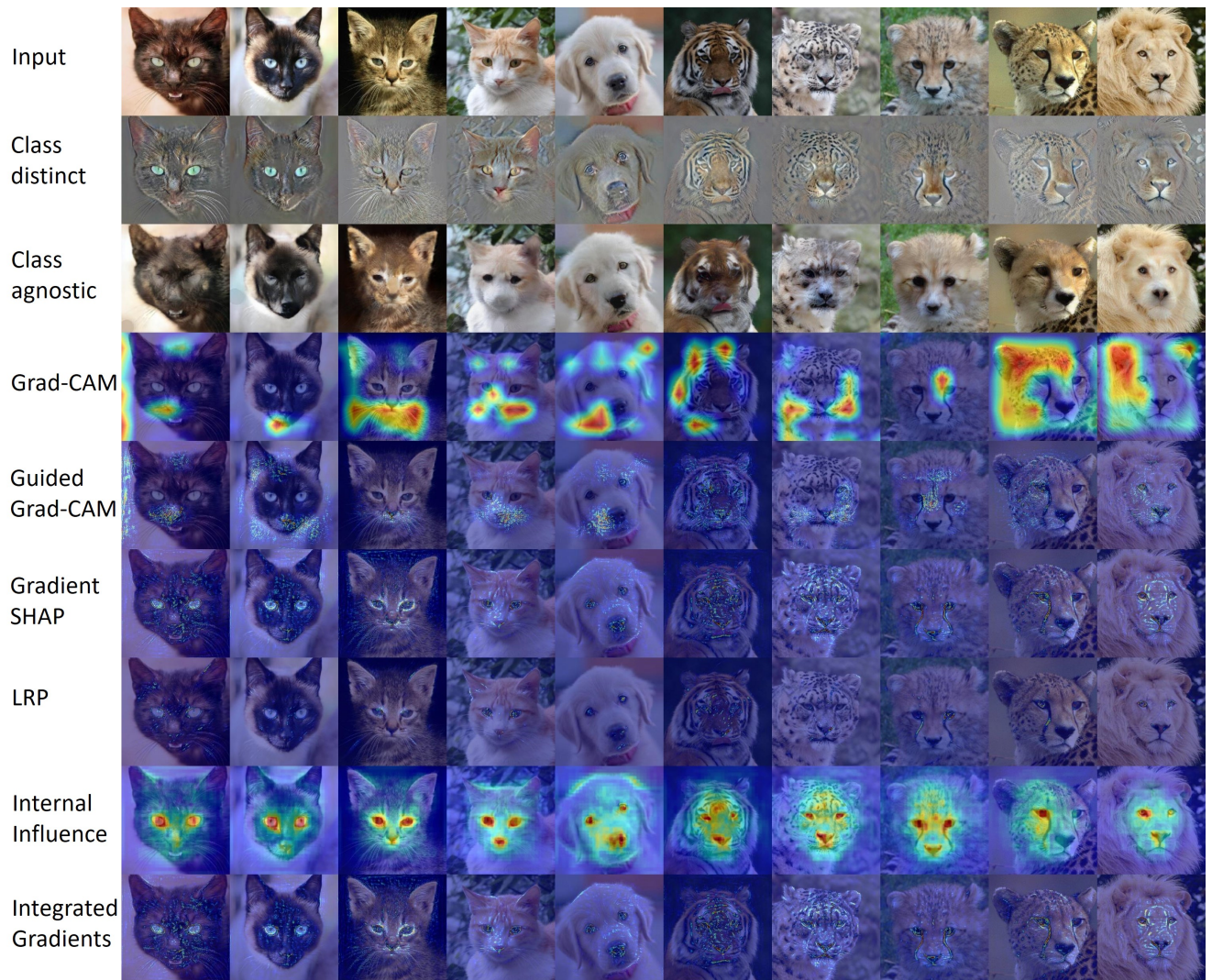


Figure 23. AFHQ animals dataset ($C = D$). Fur textures, as well as local features of eyes and nose give a full and rich explanation for class distinction. Some spurious background features appear, indicating background cues may contribute, in some cases, for the classifier’s decision.

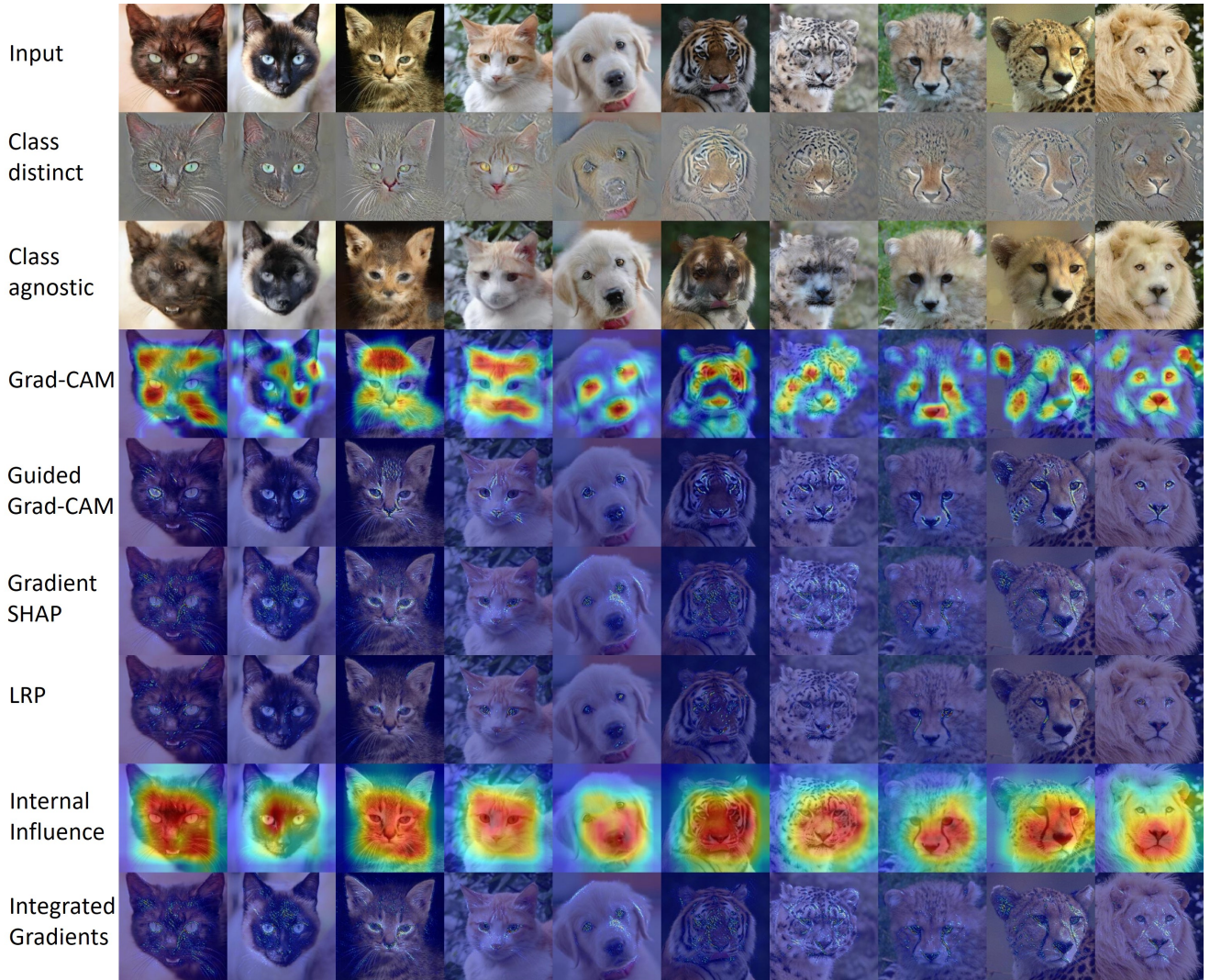


Figure 24. AFHQ animals dataset ($C = ResNet18$). Here ResNet18 is used as a classifier. Since both the discriminator and ResNet18 are highly accurate we can expect mostly similar distinct features. Whereas some XAI algorithm provide similar heatmaps, others are less stable. This depends also on meta-parameters, such as layer selection. Our algorithm shows only minor decomposition differences and appears stable.

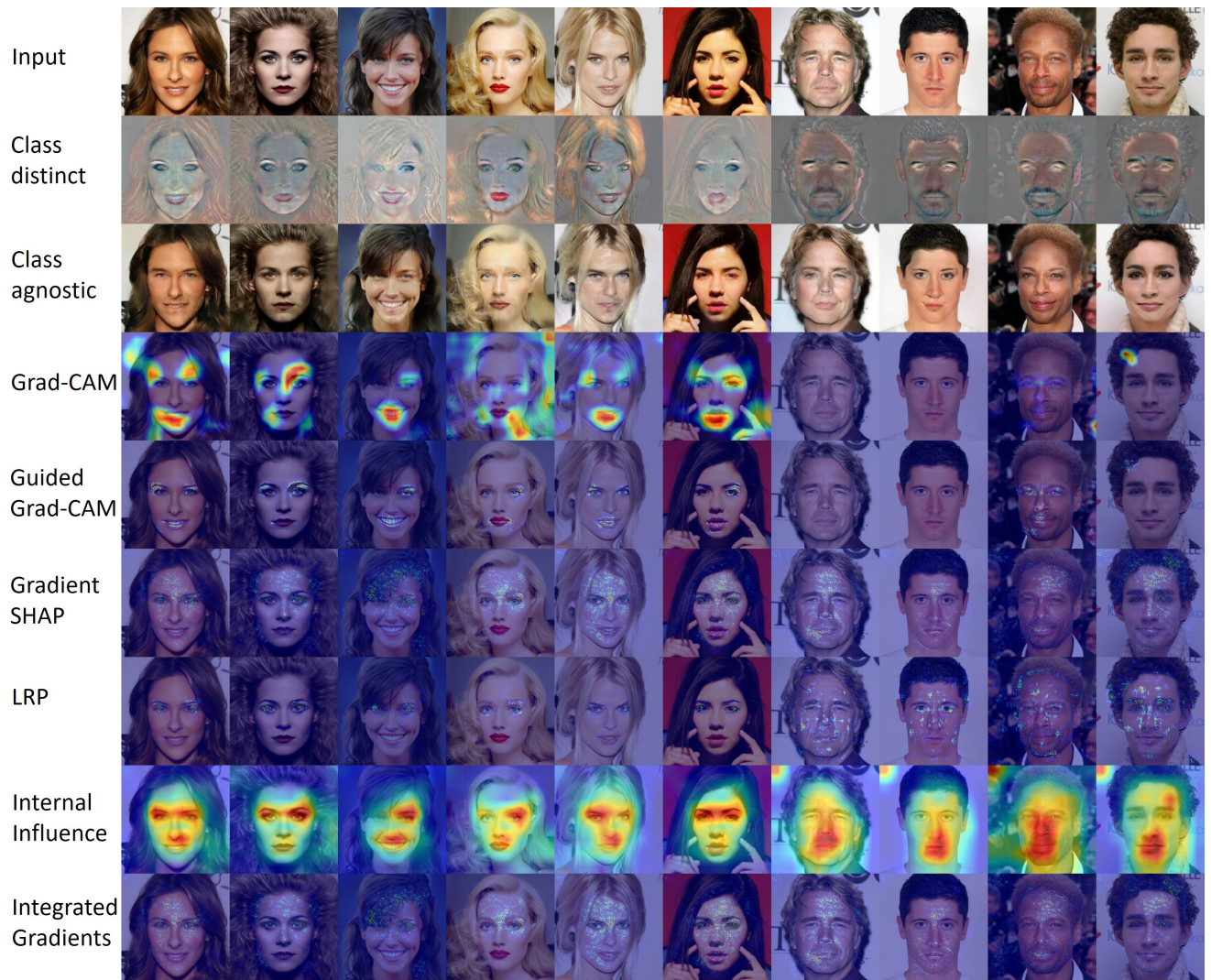


Figure 25. CelebA dataset ($C = ResNet18$).

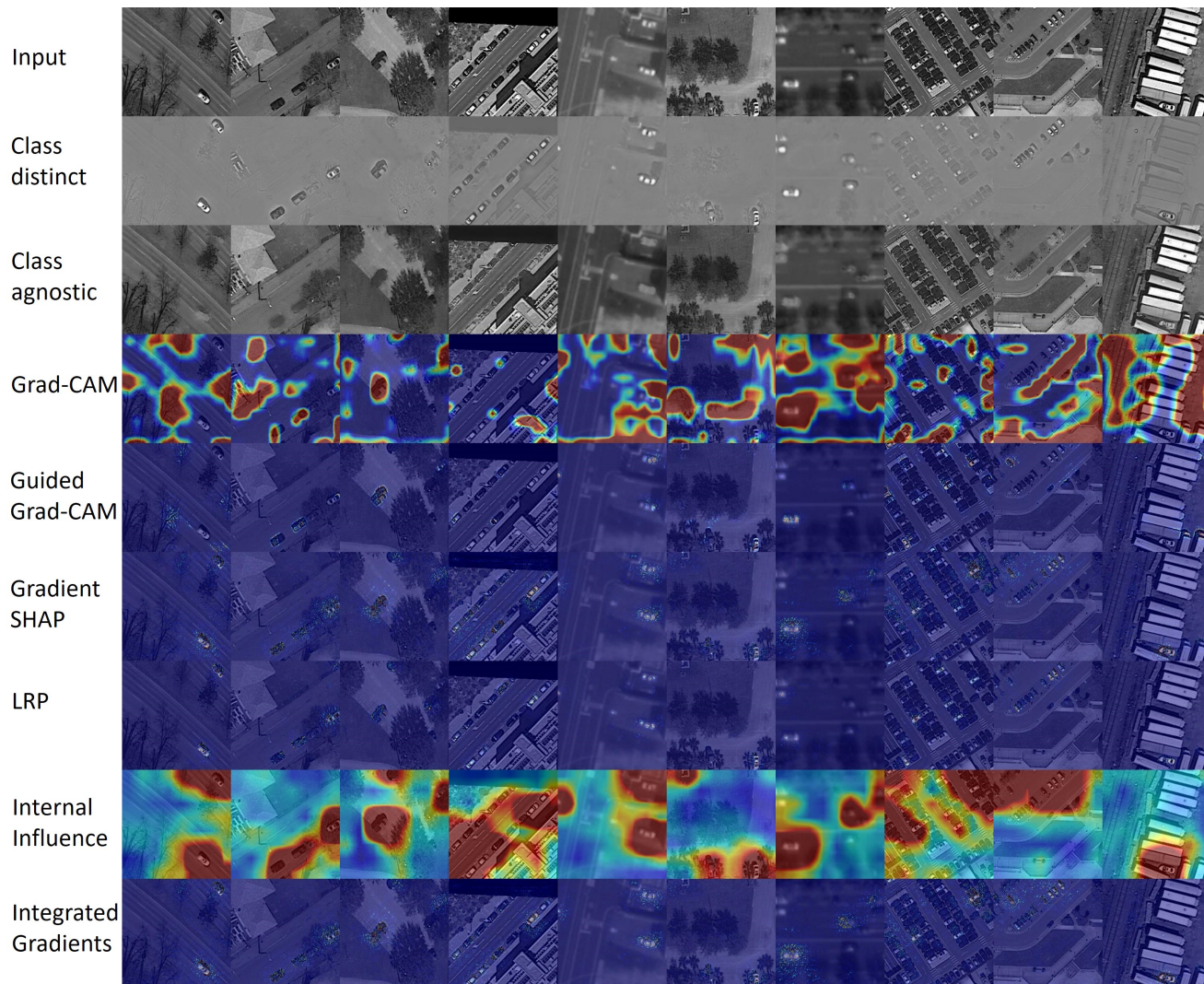


Figure 26. DOTA (cars) dataset ($C = ResNet18$).

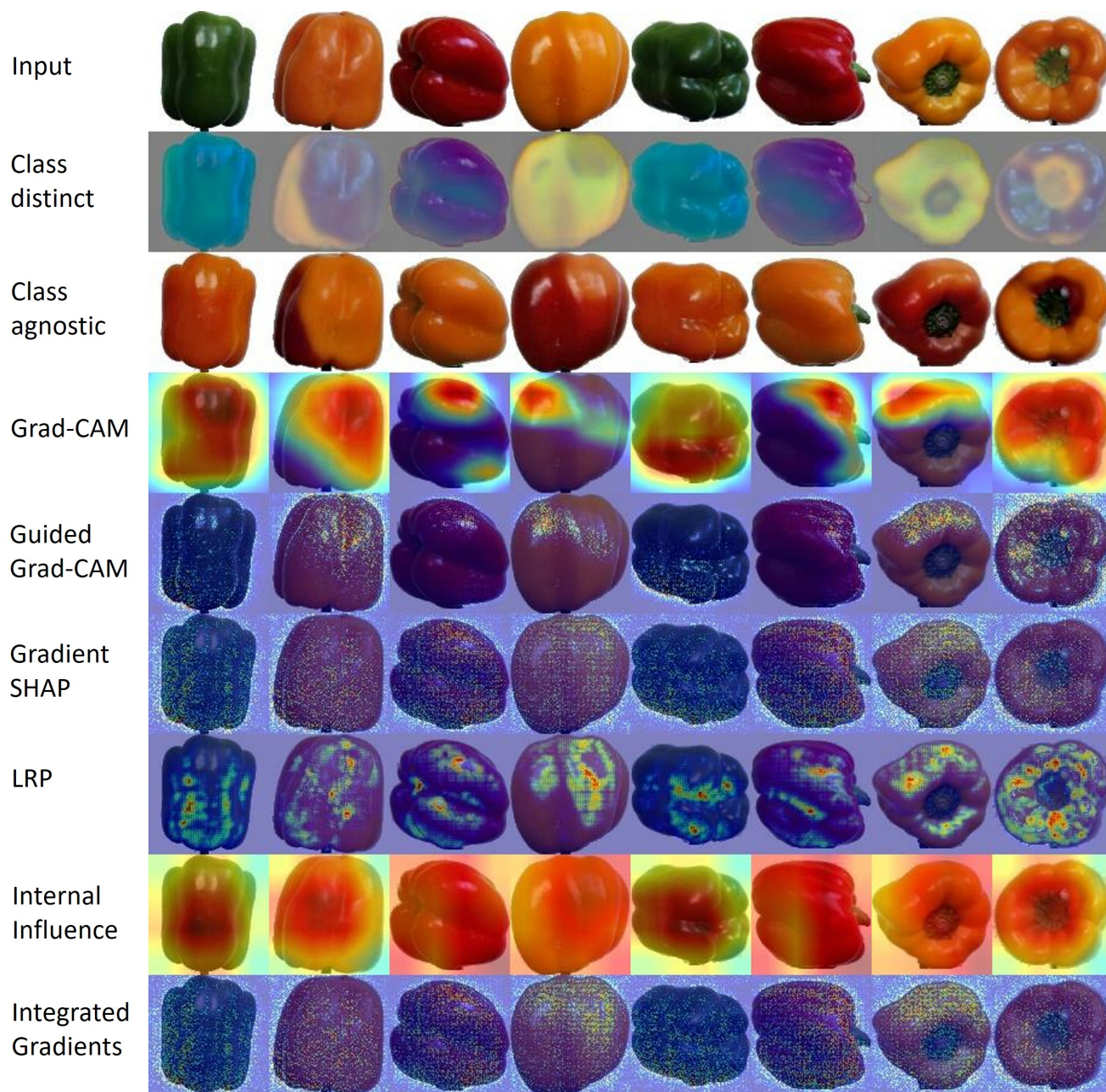


Figure 27. Peppers dataset ($C = ResNet18$). Here we get different agnostic and distinction parts, compared to the case $C = D$. However, color is still the main distinctive feature and is well visualized, compared to heatmap methods.

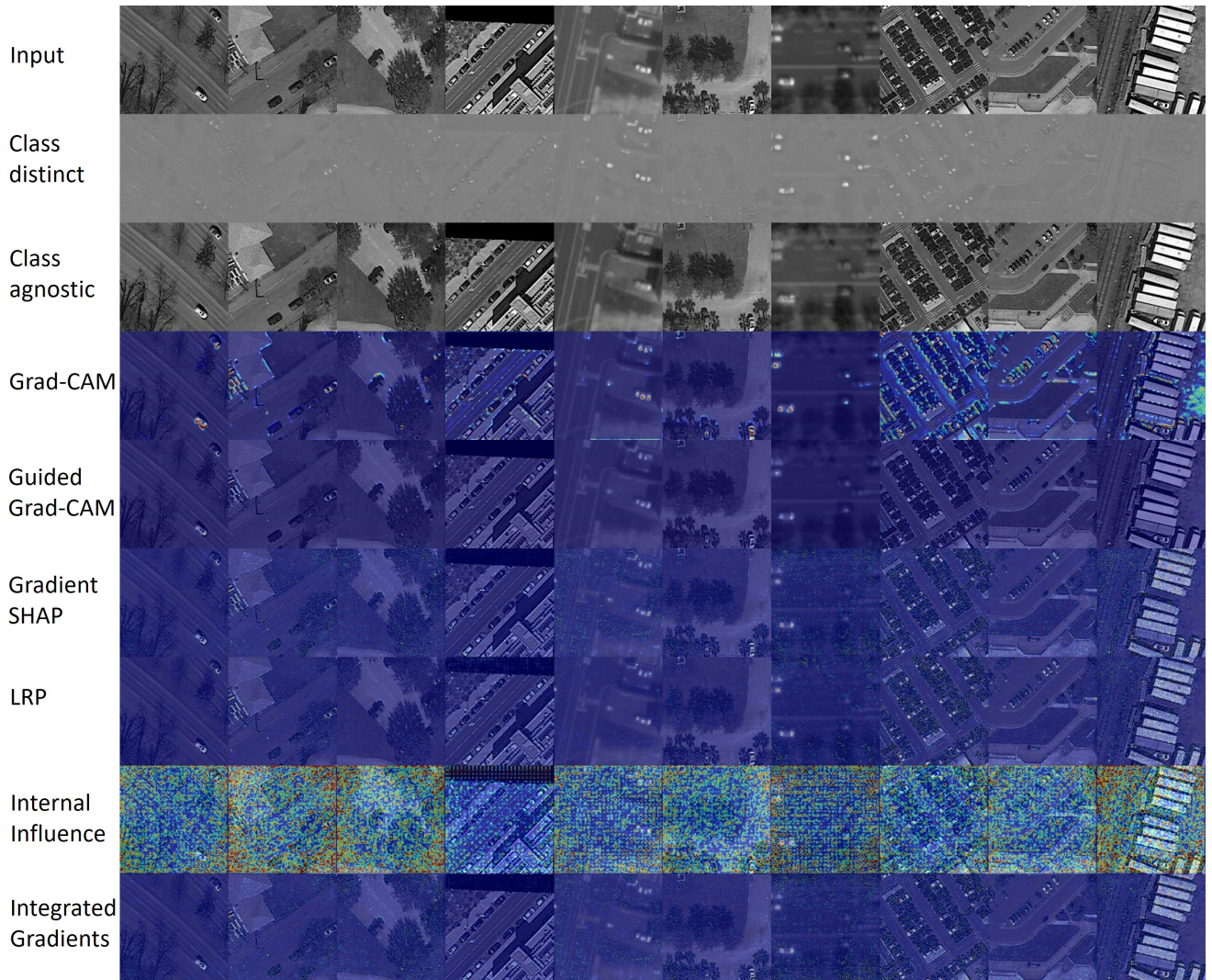


Figure 28. DOTA (cars) dataset ($C = Simple$). It can be observed that the distinction map is different and less clear compared to the maps generated by the discriminator and ResNet18. We hypothesize that this is due to the classifier’s lower accuracy percentages, leading to a less precise differentiation between important features and those that are not.

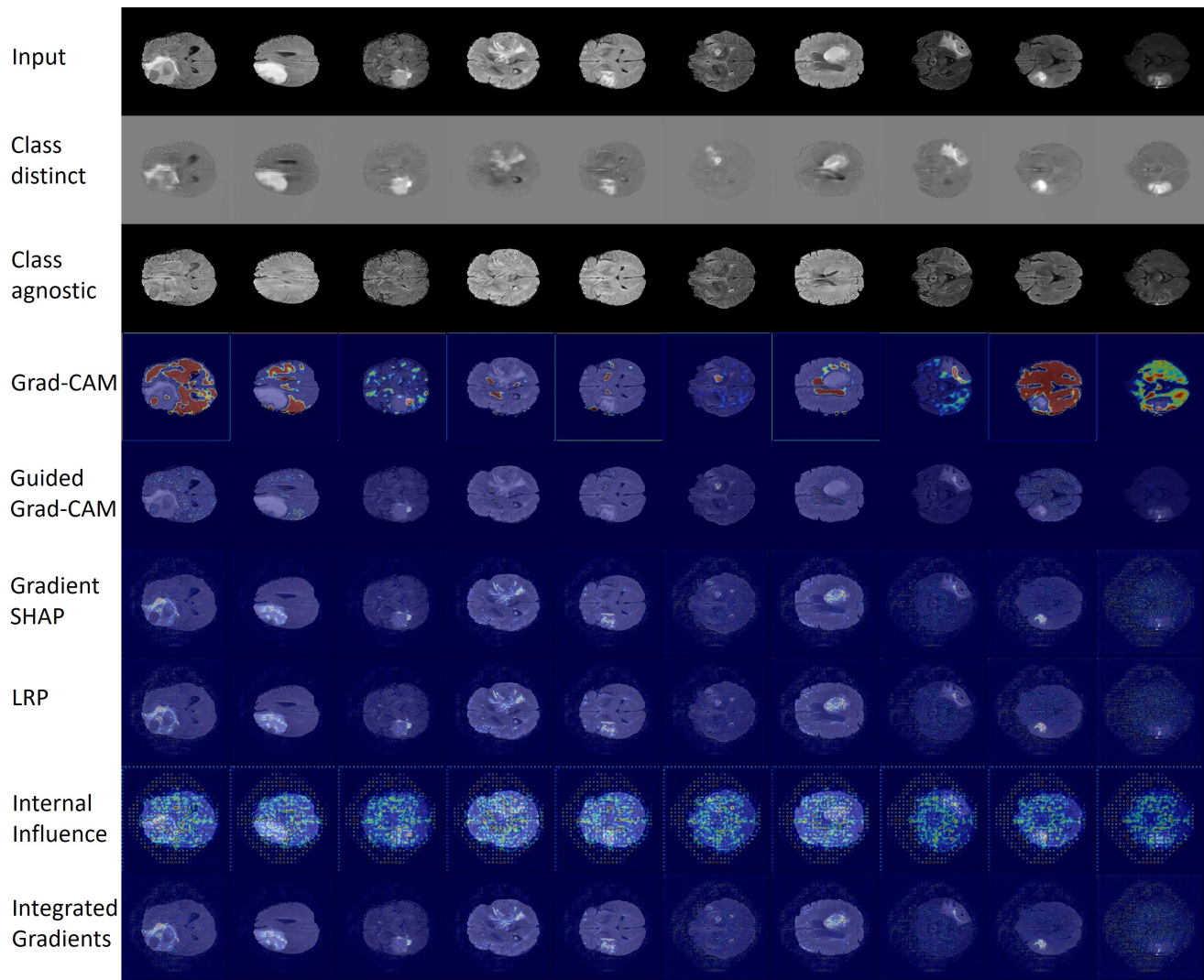


Figure 29. BraTS dataset ($C = Simple$). As in Fig. 28, here too, you can observe that the distinction maps are less clean, and we assume that this is due to similar reasons.

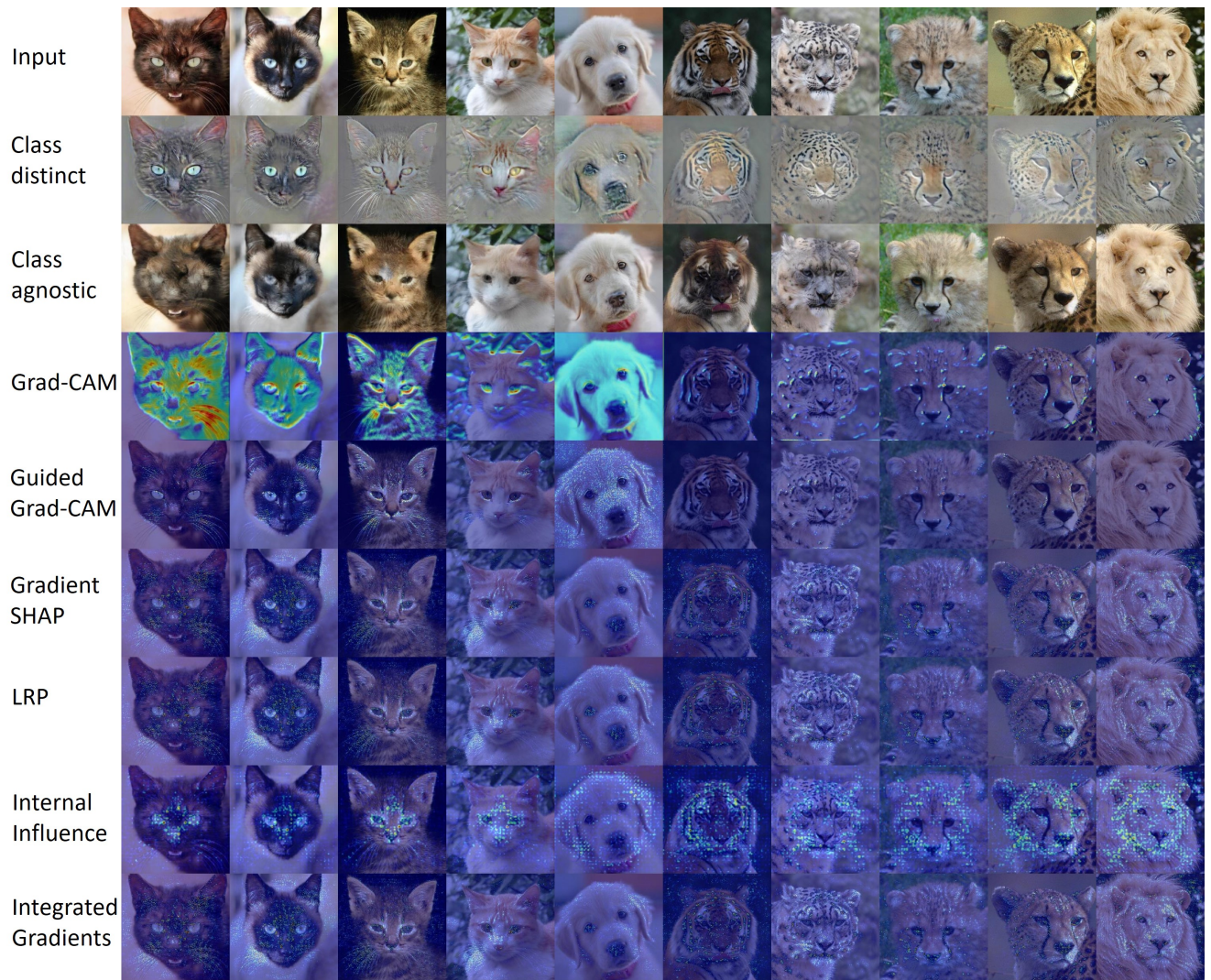


Figure 30. AFHQ dataset ($C = Simple$).

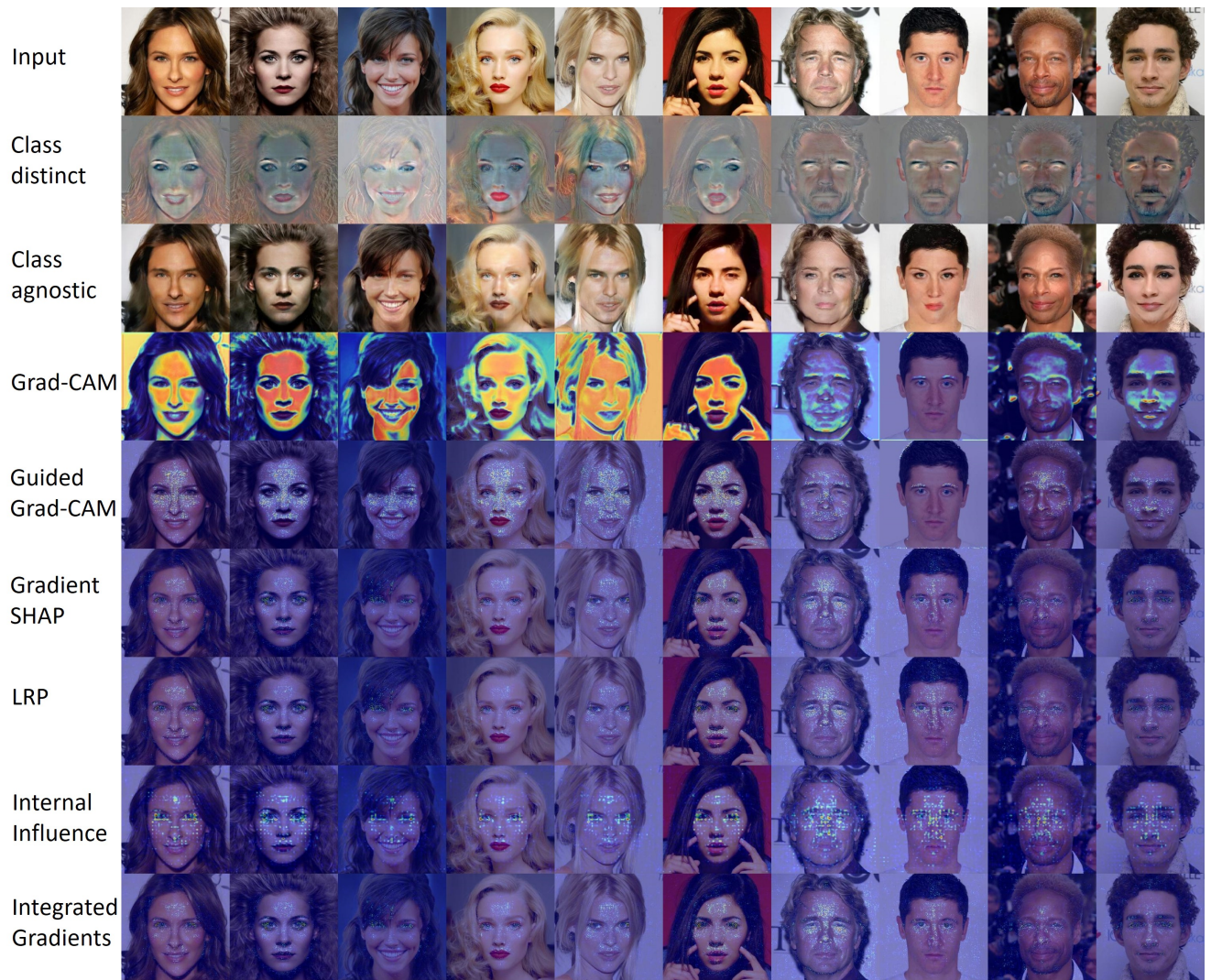


Figure 31. CelebA dataset ($C = Simple$).